

Cite this: *Mater. Adv.*, 2026,
7, 2892

Enhanced photodegradation of antibiotics using a novel BiVO₄/P-doped TiO₂ heterostructure: performance evaluation, property and kinetic modelling

Tanzim Ur Rahman,^a Musfekur Rahman Dihan,^{id}^a Abdul Hai^b and Md. Shahinoor Islam^{id}^{*a}

This study presents the performance evaluation of a novel P-doped TiO₂-BiVO₄ heterostructured photocatalyst against two model antibiotics, metronidazole (MNZ) and ciprofloxacin (CIP), in both single and binary solution system. The morphological analysis confirms the successful incorporation of anatase P-TiO₂ into monoclinic BiVO₄ and the reduction in BiVO₄ particle size with increasing surface roughness. Two multivariable linear regression models were developed to predict the crystallite sizes and bandgap of the photocatalyst. Among the seven photocatalysts, the composite with 80 wt% P-TiO₂ in BiVO₄ exhibited the highest degradation for CIP and MNZ (94.48% and 96.07%, respectively), with a crystallite size of 14 nm and an optimized bandgap of 2.59 eV. Kinetic studies revealed that the degradation followed a first-order model, with P-TiO₂/BiVO₄-80 exhibiting rate constants 4.92 and 9.50 times those of pristine TiO₂ and BiVO₄, respectively. Additionally, the estimated catalytic potential and the synergy index showed the effectiveness of coupling P-TiO₂ with BiVO₄ for potential use in AOPs. The effects of operational parameters were evaluated to identify the optimized conditions (10 ppm antibiotics, 1.2 g L⁻¹ catalyst loading, natural pH, and 20 mM H₂O₂), under which nearly complete degradation of both MNZ and CIP was achieved. Similar degradation efficiency in the binary antibiotic mixture, and while retaining 78% efficiency after five cycles, demonstrated the robustness, recyclability, and stability of the photocatalytic activity of the synthesized photocatalyst. Hence, we believe that the demonstrated insights of the proposed highly efficient novel P-TiO₂/BiVO₄ can further facilitate the transition towards sustainable wastewater treatment, providing clean and safer water for everyone.

Received 1st December 2025,
Accepted 23rd January 2026

DOI: 10.1039/d5ma01398d

rsc.li/materials-advances

1. Introduction

The demand for antibiotics to treat infectious diseases in humans and animals, including livestock and aquaculture, has increased significantly; however, a substantial portion of these antibiotics is released into the environment because only a small fraction is metabolized.^{1,2} Browne *et al.* estimated that global antibiotic consumption increased by approximately 46% between 2000 and 2018, with South Asian countries, including Bangladesh, India, Pakistan, and Nepal, accounting for about 25% of total consumption.³ This trend of rising consumption and environmental release is also linked to antimicrobial resistance (AMR), which can be detrimental to ecosystems

and public health. The threat of antibiotic pollution and the emergence of AMR is particularly high in low- to middle-income countries (LMICs) like Bangladesh, mainly due to a lack of awareness and the unregulated, over-the-counter availability of antibiotics without prescriptions. In addition to contamination from excessive use, antibiotics enter water bodies from agricultural runoff, the pharmaceutical industry, and hospital wastewater. They are also released into water bodies *via* municipal and industrial wastewater treatment plants (WWTPs), as current treatment technologies are insufficient to remove and effectively mineralize such pollutants.^{1,2,4} In Bangladesh, the most commonly used antibiotics include ciprofloxacin (CIP) and metronidazole (MNZ). In a study, Akhter *et al.* estimated that approximately 273 kg of CIP is released into the environment each year in the Chittagong Metropolitan area. They also reported the prevalence of CIP-resistant *E. coli* bacteria.⁵ On the other hand, MNZ has been detected at high concentrations across multiple sampling sites in Barisal.⁶ Antibiotics in water bodies, like other persistent

^a Department of Chemical Engineering, Bangladesh University of Engineering and Technology, Dhaka-1000, Bangladesh. E-mail: shahinoorislam@che.buet.ac.bd; Tel: +8801732782120

^b Department of Chemical & Petroleum Engineering, Khalifa University, 127788, Abu Dhabi, United Arab Emirates



organic pollutants (POPs), are challenging to mineralize using current wastewater treatment technologies. Thus, it is imperative to place greater emphasis on research into the effective elimination of POPs, such as antibiotics, from water reclamation pathways.^{7,8}

Heterogeneous photocatalysis has emerged as a sustainable option to eliminate POPs from water bodies.⁹ Photocatalytic treatment of pollutants is a type of advanced oxidation process (AOP) that degrades pollutants by generating highly reactive free radicals.² Among various semiconductor photocatalysts, TiO₂ is most widely utilized because of its low toxicity, stability, and availability.¹⁰ However, the main issue of TiO₂ is its large band gap of 3.2 eV, which limits its photoactivity under irradiation with longer wavelengths.¹¹ Therefore, doping it with metal/non-metals and the formation of a heterojunction with another photocatalyst can be utilized for effective electron-hole pair separation and inhibition of their recombination.^{12–14}

Doping of TiO₂ with non-metals (*e.g.*, P, N, and C) has become increasingly desirable because it can reduce the band gap by modifying the band structure, thereby improving photodegradation.^{15,16} Studies have shown that dopant P in TiO₂, resulted in enhanced photocatalytic degradation of organic pollutants. P-doped TiO₂ exhibits a narrower band gap, diverse surface and bulk properties, improved thermal stability, and a smaller particle size.¹⁷ Feng *et al.* synthesized P-doped TiO₂ with surface oxygen vacancies and utilized it for the degradation of CIP. The results revealed a 16.2-fold increase in the degradation rate relative to pristine TiO₂, and a reduction in the band gap to 3.02 eV.¹⁸ In another study, Gopal *et al.* synthesized P-doped TiO₂ by the sol-gel method using H₃PO₄ as the precursor. They observed the presence of a Ti–O–P bond, which is representative of the substitution of Ti⁴⁺ by P⁵⁺. Moreover, doping has resulted in a red shift of the absorption edge, a reduction in particle size, an increase in thermal stability, and inhibition of the phase transition of anatase TiO₂.¹⁹ Photocatalytic performance can be further improved by forming heterojunctions with other semiconductors, such as ZnO, BiVO₄, and SnO₂, whose suitable band structures can suppress electron-hole recombination.^{11,20,21} For instance, the coupling of TiO₂ with BiVO₄ has been studied extensively for enhanced photocatalytic performance owing to heterojunction formation, improved charge-carrier separation, and reduced recombination. Monoclinic BiVO₄, with a low band gap of approximately 2.4 eV, is prone to high electron-hole recombination, resulting in poor photocatalytic performance.²² However, this limitation can be overcome by coupling BiVO₄ with pristine or doped TiO₂. For instance, Liaquat *et al.* synthesized TiO₂/BiVO₄ *via* a hydrothermal method and used it to degrade tetracycline (TC) and methylene blue (MB). A maximum of 72% TC degradation was observed with TiO₂/BiVO₄, whereas degradation was 35% and 40% for pristine BiVO₄ and TiO₂, respectively.²³ On the other hand, MB degradation was 38% and 43% for pristine BiVO₄ and TiO₂, respectively, whereas it increased to 87% for TiO₂/BiVO₄. Moreover, studies have shown that non-metal (nitrogen and boron) doped TiO₂ coupled with BiVO₄ exhibits improved photocatalytic performance.^{24,25}

However, to the best of our knowledge, no studies have reported the photocatalytic performance of P-doped TiO₂ coupled with BiVO₄; therefore, it remains unclear whether this combination can further improve photocatalytic performance. Moreover, industrial wastewater contains multiple contaminants, and their presence can both contribute synergistically or act competitively during the photocatalytic degradation. For instance, the wastewater matrix may contain both CIP and MNZ, which differ in molecular structure and adsorption behavior and follow separate AOP-based degradation pathways.²⁶ Most studies report the photocatalytic efficiencies of the synthesized heterojunctions for single contaminants; thus, it is imperative to determine whether the material can simultaneously remove multiple pollutants, benefiting real wastewater treatment applications.

Thus, in this study, we synthesized and evaluated the photocatalytic performance of P-TiO₂/BiVO₄. Seven types of photocatalysts were synthesized, with varying mass ratios of P-TiO₂ in BiVO₄, to identify the optimal combination, and different characterization techniques, XRD, FESEM-EDX, FTIR, and UV-vis spectroscopy, were utilized for examining the structural and functional properties of the synthesized catalysts. Two multivariable linear regression (MLR) models were also proposed to predict the photocatalyst's crystallite size and bandgap from elemental composition. The photocatalytic performance evaluations were conducted against CIP and MNZ, both in single and binary mixtures, along with catalytic potential, synergy index, and kinetic studies to assess the effectiveness of the synthesized photocatalysts. The effects of various operational parameters, including solution pH, catalyst dosage, initial pollutant concentration, and hydrogen peroxide concentration, were assessed to determine the optimal operational conditions. Thus, we believe this study will provide fresh insights into the properties, effectiveness, and behavior of the novel P-TiO₂/BiVO₄ heterojunction photocatalyst developed for the degradation of antibiotics in wastewater.

2. Materials and methodology

2.1. Materials

Absolute ethanol (C₂H₅OH) (Tedia, USA), *ortho*-phosphoric acid (H₃PO₄) (Merck, Germany, 85%), titanium(IV) isopropoxide (C₁₄H₂₈O₄Ti) (Sigma-Aldrich, Germany 98%), bismuth nitrate pentahydrate (Bi(NO₃)₃·5H₂O) (Sigma-Aldrich, Germany, 98%), nitric acid (HNO₃), citric acid (C₆H₈O₇), ammonium metavanadate (NH₄VO₃) (Sigma-Aldrich, Germany, 99%), ammonium hydroxide (NH₄OH), metronidazole (C₆H₉N₃O₃), ciprofloxacin (C₁₇H₁₈FN₃O₃), and hydrogen peroxide (H₂O₂) (Sigma-Aldrich, 30% (w/w)) were used. All chemicals used for experimentation were of analytical grade.

2.2. Methodology

2.2.1. Synthesis of P-doped TiO₂. The photocatalysts were prepared using the sol-gel method following the methodology described in the published literature.^{11,27} The stoichiometric



amount of *ortho*-phosphoric acid as a phosphorus precursor was added to the 100 mL of ethanol and 60 mL of water mixture.²⁸ For the synthesis of pure TiO₂, following the addition of phosphoric acid, 15 mL of titanium(IV) isopropoxide was added dropwise with continuous stirring for 10 minutes, maintaining the pH at 3 with the addition of HNO₃. The mixture was then stirred vigorously for 3 hours and left overnight to age. The gel was separated by centrifugation at 5000 rpm for 15 minutes and then dried at 110 °C overnight. The resulting dried powder was calcined at 400 °C for 3 hours and then ground to get fine particles.

2.2.2. Synthesis of P-doped TiO₂/BiVO₄. The synthesis of P-doped TiO₂/BiVO₄ was conducted following ref. 29 and 30. In brief, 0.01 moles of Bi(NO₃)₃·5H₂O were added to 50 mL of 10% HNO₃ solution, and a clear solution was obtained by the addition of 0.02 mol citric acid (solution I). In a subsequent step, NH₄VO₃ was added to 50 mL of deionized water in an equimolar ratio with Bi(NO₃)₃·5H₂O, and the mixture was heated to 80 °C with continuous stirring to obtain a greenish-yellow solution. Citric acid was added to maintain an NH₄VO₃ to citric acid molar ratio of 2 : 1. Solution II was stirred at 80 °C until a brown-colored solution was obtained. Subsequently, solution I was added dropwise to solution II, resulting in a blue-colored solution. Stoichiometric amounts of P-doped TiO₂ were added to the constant concentration of BiVO₄ to obtain composites of three different mass ratios of P-doped TiO₂ to BiVO₄ (1 : 0.25, 1 : 1, and 1 : 4). The mixture was adjusted to pH 6.5 and was sonicated for 30 minutes to ensure better mixing and homogeneous dispersion of P-doped TiO₂ in P-doped TiO₂/BiVO₄.^{25,30} The resulting solution was dried overnight at 80 °C, calcined at 500 °C for 4 hours, and then ground to obtain a fine powder. Depending on the compositions of P-TiO₂ and BiVO₄, the composites are labeled as P-TiO₂/BiVO₄-*x*, where *x* is the theoretical mass percentage of P-TiO₂. The synthesis route is depicted in Fig. 1.

2.2.3. Characterization. Morphological characteristics of the prepared photocatalyst were examined through scanning electron microscopy (SEM) with a Zeiss Sigma 300 VP. EDX was used to analyze the atomic composition and elemental mapping of the photocatalysts. The crystallographic structure of the photocatalysts was evaluated by X-ray diffraction (XRD) utilizing the PANalytical Empyrean Series 2 X-ray diffraction system. The system was operated with Cu K α radiation at 1.54 Å, 40 mA, and 40 keV. The intensity was recorded for 2 θ values ranging from 20° to 75°. From the obtained diffractogram, the Debye–Scherrer formula was used to compute the average crystallite size of the photocatalysts, and the tetragonal system equation was used to determine the lattice parameters. UV-vis spectroscopy (300–800 nm) was performed using a Shimadzu UV-2600 with a 100 ppm suspension of photocatalysts. The Tauc plots were generated to estimate the individual band gaps of the prepared photocatalysts. FTIR (Thermo Fisher Scientific Nicolet IS7 Spectrometer) was used to identify surface functional groups, with wavenumbers ranging from 4000 cm⁻¹ to 400 cm⁻¹.

2.3. Photocatalytic activity and kinetic modelling

2.3.1. Experimental setup for the degradation evaluation. Ciprofloxacin (CIP) and metronidazole (MNZ) are among the most widely used antibiotics in Bangladesh and are detected at relatively high levels in wastewater relative to other antibiotics. In addition, they have distinct molecular structures, contrasting physicochemical properties, and different photocatalytic degradation pathways, which can also help assess the robustness of the synthesized photocatalysts against different antibiotics. Thus, for this study, we selected CIP and MNZ as model antibiotics to evaluate the photodegradation performance of the synthesized photocatalysts, both in single-antibiotic and binary-antibiotic mixtures. Photocatalytic degradation

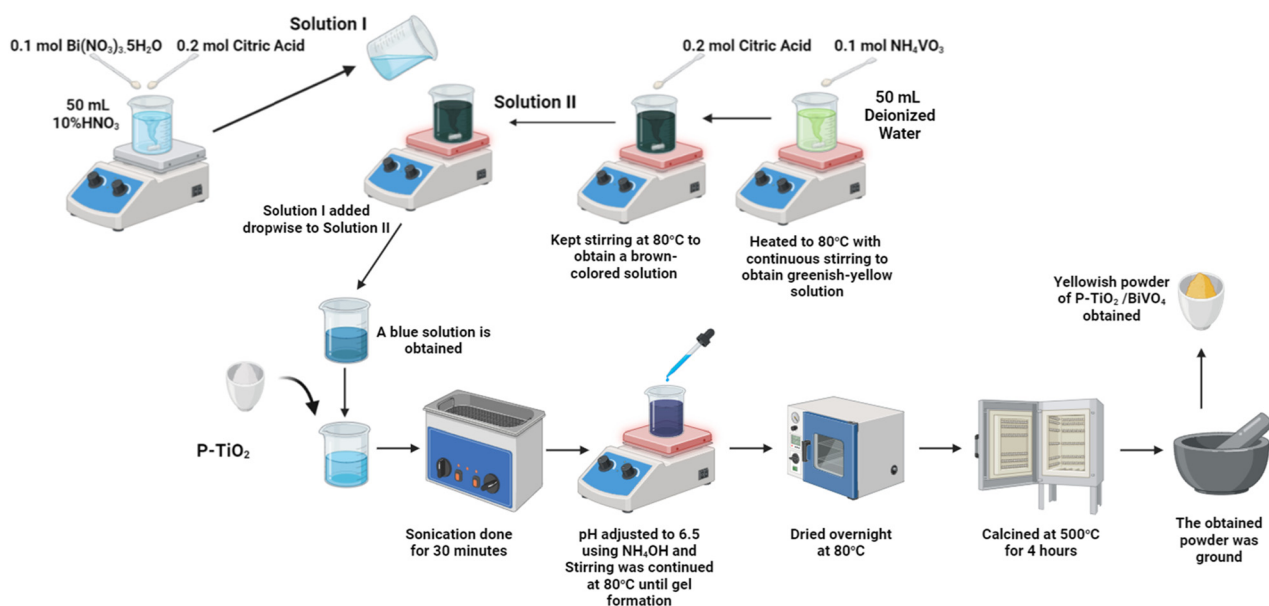


Fig. 1 Synthesis pathway of the P-TiO₂/BiVO₄ photocatalyst.



experiments were performed in 20 ppm solutions of individual CIP and MNZ, and in a binary mixture at 15 ppm each. The catalyst dose was maintained at 1 mg mL⁻¹ across all experiments, and the performance of all synthesized photocatalysts was evaluated by adding 0.1 g of catalyst powder to 100 mL of antibiotic solution. No pH adjustment was made for these tests, and to ensure the adsorption–desorption equilibrium, the catalyst-containing solution was stirred in the dark for 30 minutes. TiO₂ predominantly requires UV irradiation for photocatalytic activity, and the synthesized P-doped and BiVO₄-coupled composites have band gaps in the visible-light zone. However, band-gap narrowing alone does not guarantee efficient visible-light photocatalytic activity. Rather, P and BiVO₄-based composites are synthesized to improve charge separation and reduce recombination rates while maintaining TiO₂'s UV absorption capacity. Thus, we used UV-A irradiation in the photoreactor to test the photocatalytic performance of all the composites. Moreover, sunlight's UV fraction is dominated by UV-A, which accounts for >90% of all UV irradiation reaching the surface. Our photoreactor setup had five lamps (18 W BLB Philips) having a $\lambda_{\text{max}} = 365$ nm. After maintaining the dark conditions, the UV illumination was turned on, and the aqueous samples were collected at 30-minute intervals for up to 3 hours. For individual and binary mixtures, the concentrations of CIP and MNZ were quantified using a Shimadzu UV-2600 spectrophotometer at their respective λ_{max} values (272 nm for CIP and 320 nm for MNZ) and validated with individual calibration curves. No spectral overlap was observed under the selected wavelengths, and linearity ($R^2 > 0.99$) was maintained for both antibiotics, confirming reliable quantification without matrix interference. The degradation efficiency was calculated using the following equation.

$$\% \text{Removal} = \frac{C_0 - C}{C_0} \times 100 \quad (\text{i})$$

here, C_0 and C denote the initial and time-dependent concentrations of the antibiotics, respectively.

2.3.2. Parametric analysis and reusability. Because photodegradation strongly depended on solution pH, catalyst loading, pollutant concentration, and external oxidant dose, we also evaluated the effects of these parameters on the optimal photocatalyst. The impact of solution pH on photodegradation was studied by varying pH from 3 to 10 and to the natural pH of the antibiotics. The initial concentrations of CIP and MNZ were varied from 10 to 40 ppm to evaluate the effect of initial pollutant concentration on degradation efficiency. Photocatalyst dose was varied from 0.8 g L⁻¹ to 1.4 g L⁻¹ to identify the optimal catalyst loading for maximum degradation. The photocatalytic performance of the photocatalyst was also assessed by varying the H₂O₂ dose to determine the impact of the external oxidant on photodegradation. To evaluate the recyclability of the photocatalyst, after each photodegradation cycle, the spent photocatalyst was removed from the suspension by centrifugation at 5000 rpm for 50 minutes. After separation, the catalyst was washed with ethanol to remove any remaining impurities and then dried overnight at 80 °C for

reuse. The loss of the catalyst sample was accounted for by applying the gravimetric method.

2.3.3. Kinetic and performance modelling. Evaluation of reaction kinetics and development of a rate expression are crucial for AOP-based catalytic efficiency testing, reactor design, and process scale-up, particularly in heterogeneous catalysis, as they provide insights into the degradation mechanism, the relationship between concentration and time, and the contributions of other reactants or products to the final yield. Additionally, although heterogeneous photocatalysis typically follows first- or pseudo-first-order rate expressions derived from the Langmuir–Hinshelwood model, deviations are expected at high concentrations, during intermediate formation, and in competitive degradation in a binary mixture. Thus, it is imperative to evaluate all possible kinetic models and select the most appropriate model to avoid misinterpretation of the degradation mechanism. Therefore, the degradation data for all photocatalysts were fitted to zeroth-, first-, and second-order kinetic models to select the most suitable models and determine the rate constants (k) for CIP and MNZ degradation, both individually and in the binary mixture. The kinetic model equations are as follows:

Zero-order kinetic model:

$$C_t - C_0 = k_0 t \quad (\text{ii})$$

1st order kinetic model:

$$\ln \frac{C_0}{C_t} = k_1 t \quad (\text{iii})$$

2nd order kinetic model:

$$\frac{1}{C_t} - \frac{1}{C_0} = k_2 t \quad (\text{iv})$$

here, k_0 , k_1 , and k_2 denote the zero-order, 1st order, and 2nd order rate constants, respectively.

Furthermore, photocatalytic antibiotic degradation involves surface adsorption, the photocatalyst's oxidation under UV irradiation, and photolysis under UV irradiation alone. Thus, for this hybrid system, it is imperative to determine whether the combined processes increase overall degradation or exhibit synergistic effects. To assess this, the catalytic potential (CP), the synergy index (SI), and the relative contributions (RC) are evaluated for the synthesized photocatalyst, and the catalytic performance is compared using the equations presented.

The following equation defines the catalytic potential of the composites.

$$\% \text{Catalytic potential} = R_{(\text{catalyst}+\text{UV})} - (R_{\text{adsorption}} + R_{\text{UV}}) \quad (\text{v})$$

where R is the percentage removal of antibiotics. The synergy index (SI) is expressed by

$$\text{Synergy index (SI)} = \frac{R_{\text{UV}+\text{P-TiO}_2/\text{BiVO}_4}}{R_{\text{UV}+/\text{BiVO}_4} + R_{\text{P-TiO}_2} + R_{\text{BiVO}_4}} \quad (\text{vi})$$



The relative contribution (RC) of each process in a hybrid system is defined by

$$\% \text{Release contribution} = \frac{R_{\text{UV+catalyst or UV or adsorption}}}{R_{\text{UV+catalyst}}} \quad (\text{vii})$$

3. Results and discussion

3.1. Structural and functional properties of the synthesized photocatalysts

3.1.1. Crystallite structure and sizes of the photocatalysts.

The crystallite structures of the synthesized photocatalyst samples were analyzed using XRD patterns, as shown in Fig. 2, which exhibit characteristic peak intensities at different 2θ values. For the TiO_2 sample, XRD patterns show predominant diffraction peaks at $2\theta = 25.39^\circ$, 37.96° , 48.14° , and 53.83° , corresponding to the crystal phases (100), (004), (200), and (105), respectively. This confirms the presence of the pure anatase phase in the sample as per JCPDS Card No. 21-1272.¹¹ No distinguishable peaks associated with phosphorus (e.g., phosphorus oxides) are found due to the uniform dispersion and small amounts of dopants present in the sample,³¹ resulting in the XRD patterns of the TiO_2 sample and P-TiO₂ being the same (Fig. 2a and b). Moreover, the peak intensities of P-TiO₂ are found to be lower than those of pure TiO_2 . This reduction in crystallite size can be attributed to the incorporation of P atoms into the TiO_2 structure. The ionic radius of P^{5+} is 0.35 Å, whereas the radii of Ti^{4+} and O^{2-} ions are 0.68 Å and 1.32 Å. P doping results in crystal defects arising from the

partial substitution of Ti^{4+} atoms, thereby lowering the average crystallite size.³²

The major diffraction peaks at $2\theta = 18.68^\circ$, 19° , 28.3° , and 30.61° , corresponding to crystallite phases (101), (011), (114), and (004), indicate the presence of a monoclinic crystallite of BiVO_4 .²⁰ These major peaks and other diffraction peaks comply with the JCPDS Card No. 75-1866 of monoclinic BiVO_4 . The absence of any peaks other than those corresponding to the crystalline phases of TiO_2 and BiVO_4 in the XRD pattern suggests that there are no detectable impurities present. The peak intensity of anatase- TiO_2 at phase (100) is also observed to be reduced with an increasing amount of BiVO_4 content in the sample, as evident in Fig. 2.

The estimated average crystallite size of the synthesized photocatalysts, as well as the obtained lattice parameters (a and c), are tabulated in Table 1, where the average crystallite size was calculated using the Debye-Scherrer equation. Notably, the values of lattice parameters a and c are pretty close to the theoretical values of the JCPDS cards of the components. The crystallite size of TiO_2 was found to be 9.02 nm, which was reduced to 6.04 nm upon P doping, and the average crystallite size increased after coupling with BiVO_4 . The crystallite sizes of P-TiO₂/BiVO₄-20, P-TiO₂/BiVO₄-50, and P-TiO₂/BiVO₄-80 were 24.67 nm, 19.65 nm, and 13.99 nm, respectively. These larger crystallite sizes are attributable to the higher crystallinity of BiVO_4 (44.89 nm) and its larger atomic radius.

3.1.2. Optical properties. To investigate the optical properties of the prepared samples, the absorbance and reflectance spectra of the photocatalyst samples were analyzed over the range 300–700 nm, as shown in Fig. S1. As is evident, P doping shifted the absorption edge of TiO_2 to longer wavelengths. The addition of BiVO_4 to P-TiO₂ resulted in a redshift of the absorption edge to 400–550 nm, indicative of electron-hole pair separation upon irradiation with lower energy. To determine the optical bandgap, the indirect electron transition was considered when developing Tauc plots for the synthesized photocatalyst. From the Tauc plots shown in Fig. S2, the band gaps are determined and tabulated in Table 1. A reduced bandgap of TiO_2 , from 3.15 eV to 2.88 eV, was observed with P doping. The bandgap of the prepared TiO_2 falls in the range of typical values of TiO_2 referred to in the literature.^{11,27,33} The band gap of pristine BiVO_4 was lower than that of the others and was estimated to be 2.31 eV. Thus, the incorporation of BiVO_4 into P-TiO₂ has resulted in the reduction of the band gap of P-TiO₂ as apparent from the band gap range of P-TiO₂/BiVO₄- x (2.38 eV–2.59 eV). The reduced band gap indicates that the heterojunction between P-TiO₂ and BiVO_4 promotes efficient charge-carrier separation and suppresses electron-hole recombination. This improvement enhances the photocatalytic performance of the composites under visible light irradiation. It is also evident from the summarized data in Table 1 that the band gap of $\text{TiO}_2/\text{BiVO}_4$ - x decreased as the TiO_2 proportion decreased. This low band gap can also promote recombination of photogenerated electron-hole pairs.

3.1.3. Functional properties. The FTIR spectra of the prepared photocatalyst samples in the range 400–4000 cm^{-1} are

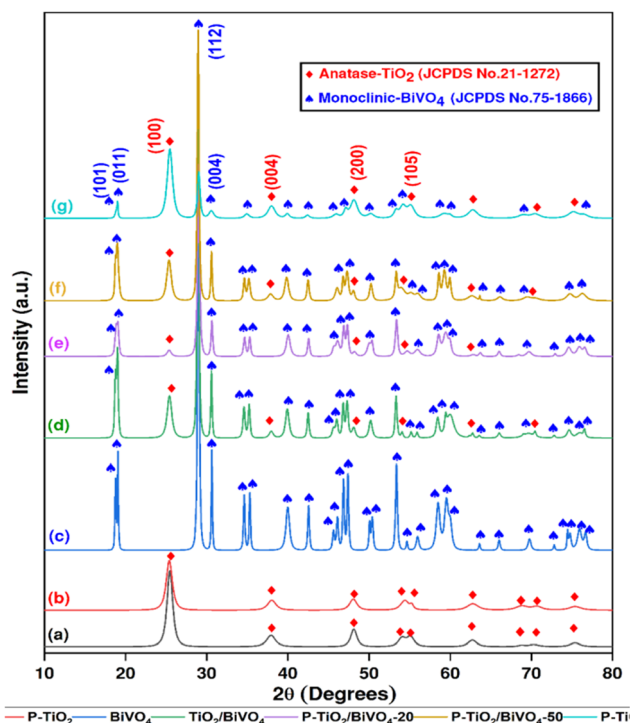


Fig. 2 The XRD patterns of the synthesized photocatalyst samples.



Table 1 Average crystallite size, lattice parameters, band gap, average particle size, and elemental compositions of photocatalyst samples

Catalysts	Average crystallite size from XRD (nm)	Lattice parameters, Å ^o		Band gap (eV)	Average particle size from ImageJ (nm)	Elemental composition (wt%)				
		<i>a</i>	<i>c</i>			Ti	O	P	Bi	V
TiO ₂	9.02	3.5124	9.7827	3.15	59.94 ± 22.71	62.75	37.25	—	—	—
P-TiO ₂	6.04	3.4977	9.4543	2.88	56.12 ± 41.87	53.53	45.53	0.94	—	—
BiVO ₄	44.89	5.1841	11.678	2.31	292.60 ± 143.11	—	9.13	—	73.38	17.49
TiO ₂ /BiVO ₄	24.89	3.506	11.688	2.63	115.95 ± 74.19	15.06	18.12	—	52.34	14.48
P-TiO ₂ /BiVO ₄ -20	24.67	3.513	11.671	2.38	152.01 ± 131.32	5.03	10.32	0.11	64.96	17.16
P-TiO ₂ /BiVO ₄ -50	19.65	3.506	11.673	2.45	105.7 ± 53.78	22.71	50.53	0.36	48.53	12.63
P-TiO ₂ /BiVO ₄ -80	13.99	3.499	11.650	2.59	61.43 ± 19.55	44.26	29.61	0.92	17.03	4.76

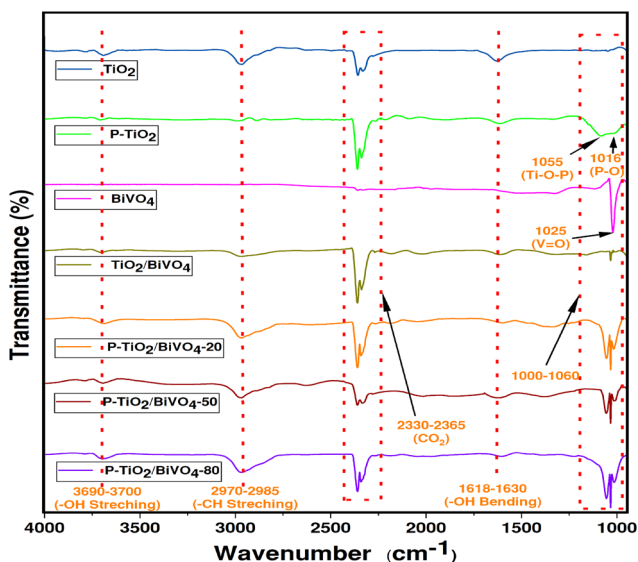


Fig. 3 FT-IR spectra of the composite photocatalyst samples for wavenumbers ranging from (a) 400 to 4000 cm⁻¹ and (b) from 1000 cm⁻¹ to 4000 cm⁻¹.

shown in Fig. 3, which are analyzed to detect functional groups and bond formation. The broad transmittance band in the region of 400 cm⁻¹ to 1000 cm⁻¹ indicates (Fig. 3a) the presence of Ti-O, Bi-O, and V-O bonds.²⁵ The peak at 615–620 cm⁻¹ indicates the presence of the functional group VO₄³⁻ in photocatalysts containing BiVO₄. The sharp peak at 1025 cm⁻¹ (Fig. 3b) is indicative of the stretching vibration of the unshared V=O bond,³⁴ which is present in all samples containing BiVO₄. For the samples having P as the dopant, two common peaks at 1016 cm⁻¹ and 1055 cm⁻¹ mark the presence of Ti-O-P stretching and P-O bonds, respectively.³¹ Thus, the presence of a Ti-O-P bond indicates the successful incorporation of P in the lattice of TiO₂, substituting Ti⁴⁺, and the presence of P-O vibration indicates the coordination of the phosphate ion with TiO₂.^{31,35} Along with these, two weak absorbance peaks are observed at 1618–1630 cm⁻¹ and 3690–3700 cm⁻¹, and the twin peaks in the range of 2330–2965 cm⁻¹ are also marked. These indicate the bending and stretching vibrations of O-H molecules present due to the adsorbed water molecule on the surface of the photocatalysts and the presence of adsorbed CO₂ molecules.³⁶

3.1.4. Surface morphology and elemental mapping. The FESEM images at 50 kx magnification, associated with EDX,

as shown in Fig. 4 and Fig. S4–S9, reveal the surface morphology and the elemental mapping of the synthesized photocatalyst samples. The particle size distributions and average particle sizes of the samples, measured using ImageJ from FESEM images of the photocatalysts, are also shown in Fig. S3. For pristine TiO₂, the average particle size was found to be 59.94 ± 22.71 nm, whereas the particle size was reduced to 56.12 ± 41.87 nm for P-TiO₂. However, the TiO₂ and P-TiO₂ particles were agglomerated and clustered, as shown in Fig. 4(a) and (b), and given the low P doping, the particle size reduction was not significant (approximately 5%), which may also be due to measurement error. The average particle size of undoped BiVO₄ is found to be 292.60 nm, with particles exhibiting well-defined spheroidal morphology and a smooth surface topology. The introduction of TiO₂ into BiVO₄ resulted in a rougher surface (Fig. 4d). As the percentage of P-TiO₂ in P-TiO₂/BiVO₄ increased, the particle size, as well as the surface roughness, increased. This is a desirable property, as surface roughness can increase the number of available active adsorption sites.

The EDX elemental mappings and the spectra (Fig. 4 and Fig. S4–S9) of the photocatalysts further confirm the successful doping of P in TiO₂ and the incorporation of P-TiO₂ in the final P-TiO₂/BiVO₄ photo-composites. For instance, in Fig. S5, the color map and spectra confirm the presence of P in P-TiO₂, with an estimated amount of approximately 1%. Additionally, EDX elemental mapping of the P-TiO₂/BiVO₄-80 sample shows a homogeneous elemental distribution (Fig. 4), and the spectra confirm the presence of Ti, O, Bi, V, and P contents in the composite. Moreover, the absence of additional peaks aside from these confirms the absence of probable impurities, as indicated by the XRD analysis. The elemental compositions obtained by EDX mapping for all samples are provided in Table 1, and it is clear that the Ti and P contents increase, whereas the Bi content decreases, as the TiO₂ content in the P-TiO₂/BiVO₄ photo-composite increases. Also, a comparison of elemental mappings in Fig. S8 and S9, and Fig. 4 shows an increase in P content in the synthesized P-TiO₂/BiVO₄ composites as the amount of P-TiO₂ in the matrix increased. The resulting elemental composition was close to the expected values. It is also noteworthy that the P content in the P-TiO₂/BiVO₄-80 sample is found to be close to that in P-TiO₂. In P-TiO₂/BiVO₄-80, P-TiO₂ is expected to constitute 80% of the total mass, and thus the P content should be lower than 0.90%. However, Fig. 4 shows higher P content in the elemental mapping of the P-TiO₂/BiVO₄-80 sample than that in P-TiO₂ shown in Fig. S5.



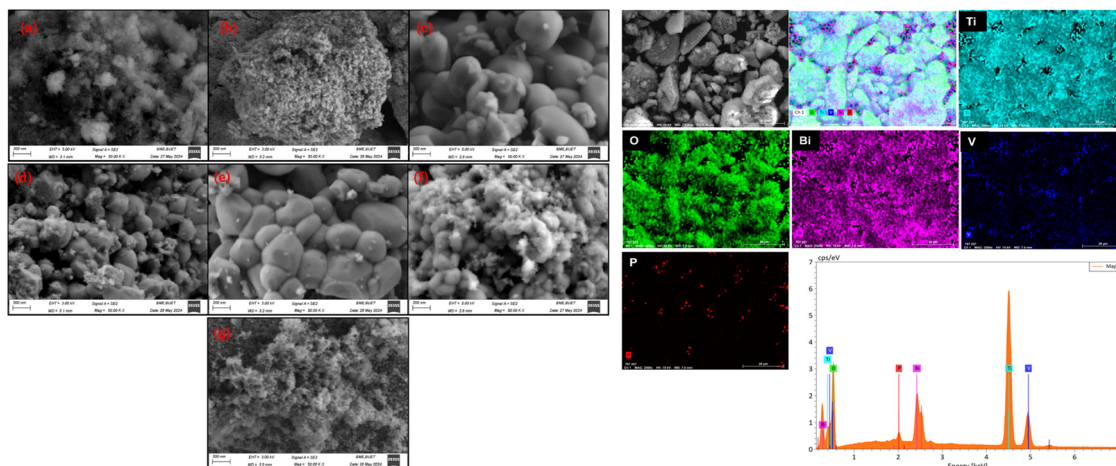


Fig. 4 FESEM images of TiO_2 (a), P-TiO_2 (b), BiVO_4 (c), $\text{TiO}_2/\text{BiVO}_4$ (d), $\text{P-TiO}_2/\text{BiVO}_4-20$ (e), $\text{P-TiO}_2/\text{BiVO}_4-50$ (f), and $\text{P-TiO}_2/\text{BiVO}_4-80$ (g). The colorful portion shows the EDX mapping and spectra of $\text{P-TiO}_2/\text{BiVO}_4-80$.

EDX is a standardless semi-quantitative analysis, and due to the selection of different surfaces with non-homogeneous elemental distribution, the obtained elemental composition may differ from the bulk composition. However, our target of successful incorporation and availability of P, TiO_2 , and BiVO_4 in the final composites has been achieved, as further supported by the XRD, FTIR, and UV-vis analyses discussed.

3.2. Regression models for predicting the crystallite size and bandgap

Furthermore, a multivariable linear regression (MLR) model for the synthesized photocatalyst was developed to predict the average crystallite size and bandgap as functions of the photocatalyst's atomic composition. MLR models provide a lower-dimensional estimate of a single dependent variable using multiple independent variables. Here, we set the average crystallite size and the band gap as the main predictive variables. The individual atoms (P, Ti, O, Bi, *etc.*) present in the synthesized photocatalyst play a significant role in determining the crystallite size and band gap, as discussed in Section 3.1. To reaffirm the collinearity between the crystallite size and the bandgap and the individual atomic compositions of the seven prepared photocatalysts (Table 1), Pearson correlation matrices are constructed (Table 2) for both the crystallite size and the bandgap. In general, the parametric Pearson correlation coefficient, $\rho \geq \pm 0.8$, indicates a stronger linear relationship between two variables, either by positive or negative means, whereas $\rho \geq \pm 0.6$ and $\rho \geq 0.3$ are considered moderately firm and fair relationships. Table S1 presents the parametric two-tailed Pearson correlation matrices between the crystallite size

and the bandgap for the five atomic component compositions (Ti, P, Bi, V, and O). From there, it is clear that the average crystallite size is strongly statistically correlated with Bi and V and negatively with Ti, that is, the higher the Ti concentration, the smaller the average crystallite size; conversely, the higher the Bi concentration, the larger the average crystallite size. This is also stated in Section 3.1, in accordance with the atomic size. For the bandgap, strong statistical correlations are observed across the same Ti, Bi, and V compositions, with Ti positively correlated and Bi and V negatively correlated. As Ti composition in the catalyst increases, the bandgap increases. The developed MLR models are presented in Table 2, along with the fitting performance indicators (R^2 , RMSE, and MSE). The predicted bandgap and crystallite sizes from the MLR models, compared with the actual values, are shown in Fig. 5(a) and (b). The R^2 values for both models are excellent: 0.958 and 0.999 for the crystallite size and bandgap, respectively. Thus, it is evident that these MLR models are effective for predicting the bandgap and crystallite size from the elemental compositions of the photocatalysts, which may further support property optimization.

3.3. Photocatalytic activity assessment and modelling

3.3.1. Performance evaluation of the photocatalysts. The photocatalytic performance of the seven synthesized photocatalytic samples (TiO_2 , P-TiO_2 , BiVO_4 , $\text{TiO}_2/\text{BiVO}_4$, $\text{P-TiO}_2/\text{BiVO}_4-20$, $\text{P-TiO}_2/\text{BiVO}_4-50$, and $\text{P-TiO}_2/\text{BiVO}_4-80$) was evaluated for the photodegradation of CIP and MNZ. The photocatalytic degradation efficiency of the catalyst was measured at the natural pH of the CIP/MNZ, with an initial concentration of

Table 2 The multivariable linear regression models of the crystallite size and the bandgap of the synthesized photocatalyst, with the performance indicators (R^2 value, RMSE, and MSE)

Predictive variable	Predictor variable	MLR models	Performance statistics
Crystallite size (nm)	Atomic compositions of Ti, O, P, Bi, and V	$\text{CS} = 8.30 + 0.134\text{Ti} - 0.183\text{O} - 0.438\text{P} + 1.933\text{Bi} - 6.005\text{V}$	$R^2: 0.958$; RMSE: 6.502; MSE: 42.27
Band gap (eV)		$\text{BG} = 4.269 - 0.0186\text{Ti} + 0.00168\text{O} - 0.485\text{P} - 0.0284\text{Bi} + 0.0066\text{V}$	$R^2: 0.999$; RMSE: 0.022; MSE: 0.0005



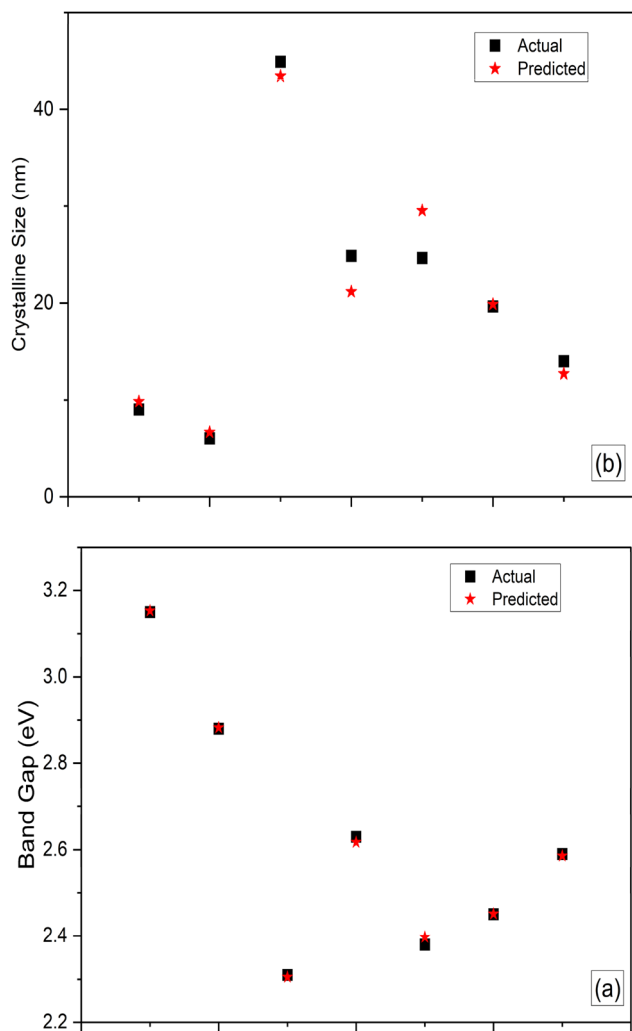


Fig. 5 The predicted bandgap (a) and crystallite size (b) values of the photocatalysts from the developed MLR models.

20 ppm and a catalyst dose of 1 g L^{-1} . Fig. 6(a and c) illustrates the %degradation of CIP and MNZ with time, respectively, for the seven catalysts, and a blank degradation was run for both CIP and MNZ under UV irradiation. UV photolysis degrades CIP and MNZ by 8.51% and 9.51%, respectively, over 180 minutes, indicating the ineffectiveness of UV treatment for recalcitrant pollutant-contaminated water. However, all seven catalysts outperformed the UV photolysis. The adsorption-desorption equilibria for all catalysts were achieved in 30 minutes under dark conditions. For CIP, initial adsorption ranged from approximately 15% to 23% for the catalysts (Fig. 6a). BiVO_4 has a comparatively lower adsorption capacity due to fewer adsorption sites and lower surface area than its TiO_2 counterparts.²³ In contrast, all the $\text{P-TiO}_2/\text{BiVO}_4$ composites have a higher adsorption capacity ($\geq 21.5\%$), benefiting from the coupling of TiO_2 and BiVO_4 . This trend is also observed for MNZ degradation (Fig. 6c). The same adsorption pattern is found for MNZ degradation. BiVO_4 had the lowest adsorption capacity, whereas the composites adsorbed a comparatively higher amount of MNZ. The final degradation efficiency of

photocatalysts follows the order: $\text{BiVO}_4 < \text{TiO}_2 < \text{P-TiO}_2 < \text{TiO}_2/\text{BiVO}_4 < \text{P-TiO}_2/\text{BiVO}_4\text{-20} < \text{P-TiO}_2/\text{BiVO}_4\text{-50} < \text{P-TiO}_2/\text{BiVO}_4\text{-80}$, both for CIP and MNZ upon 180 minutes of treatment. The degradation efficiency of pristine BiVO_4 was the lowest (39.12% and 40.18% for CIP and MNZ), owing to its low band gap of 2.31 eV, which results in a higher electron-hole recombination rate. While TiO_2 exhibited higher degradation efficiencies than BiVO_4 for both CIP and MNZ (51.92% and 52.45%, respectively), doping with P increased the efficiency only to 7% and 5% for CIP and MNZ, respectively. Pristine TiO_2 had a bandgap of 3.15 eV, requiring higher photocatalytic activation energy; however, its lower recombination rates relative to BiVO_4 and the higher surface roughness of TiO_2 and P-TiO_2 increased pollutant uptake and, consequently, higher degradation efficiency. While P doping reduced the bandgap of TiO_2 to 2.88 eV, which is expected to enhance the utilization of UV irradiation and increase the number of photogenerated electrons, overall degradation didn't improve substantially. This may be attributed to the similar adsorption rates observed for TiO_2 and P-TiO_2 , for both CIP and MNZ. This also affirms that bandgap reduction doesn't always result in higher degradation; surface adsorption can be the controlling factor in overall degradation. However, upon coupling TiO_2 with BiVO_4 , degradation increased to 15% and 17% for CIP and MNZ, respectively. Here, the composite benefited from a reduced bandgap, thereby providing more photogenerated electrons and enhanced adsorption from increased surface roughness, as evidenced by SEM analysis and bandgap measurements. This is also observed in the study reported in ref. 23, in which the $\text{TiO}_2/\text{BiVO}_4$ composite exhibited 37% and 30% higher tetracycline degradation than pristine BiVO_4 and TiO_2 , respectively. A similar study was reported in ref. 14 showed a 40% increase in CIP photodegradation by forming a $\text{NiSe}_2/\text{MoS}_2$ -based n-n heterojunction, compared with MoS_2 , and attributed the enhanced activity to material realignment of the band structure, visible-light-induced charge-carrier generation, and improved charge-carrier separation.

As noted, P-TiO_2 can increase the number of active sites, enhance electron transfer (due to an altered crystalline structure), and increase photoelectron generation (by lowering the bandgap); its coupling with BiVO_4 is expected to further improve the degradation of CIP and MNZ. This is observed for the $\text{P-TiO}_2/\text{BiVO}_4\text{-}x$ composites, which exhibited higher degradation capacity for both CIP and MNZ than the constituents, P-TiO_2 , BiVO_4 , or $\text{TiO}_2/\text{BiVO}_4$. For instance, $\text{P-TiO}_2/\text{BiVO}_4\text{-50}$ showed 50.6% and 30.6% higher CIP and MNZ degradation than BiVO_4 and TiO_2 , respectively. A similar trend is found for 20% and 80% composites. In the $\text{P-TiO}_2/\text{BiVO}_4$ composite, the shortcomings of both TiO_2 and BiVO_4 are offset by each other. For instance, the bandgap of TiO_2 is reduced by BiVO_4 , thereby increasing the utilization of incident light and thereby increasing the number of photogenerated electron-hole pairs, whereas P-TiO_2 improves the mobility of photogenerated electrons and enhances adsorption through increased surface roughness. This trend is also reported in ref. 2, where the lowered bandgap of $\text{NiSe}_2/\text{WO}_3$ (2.66 eV) and the suppression of rapid electron-



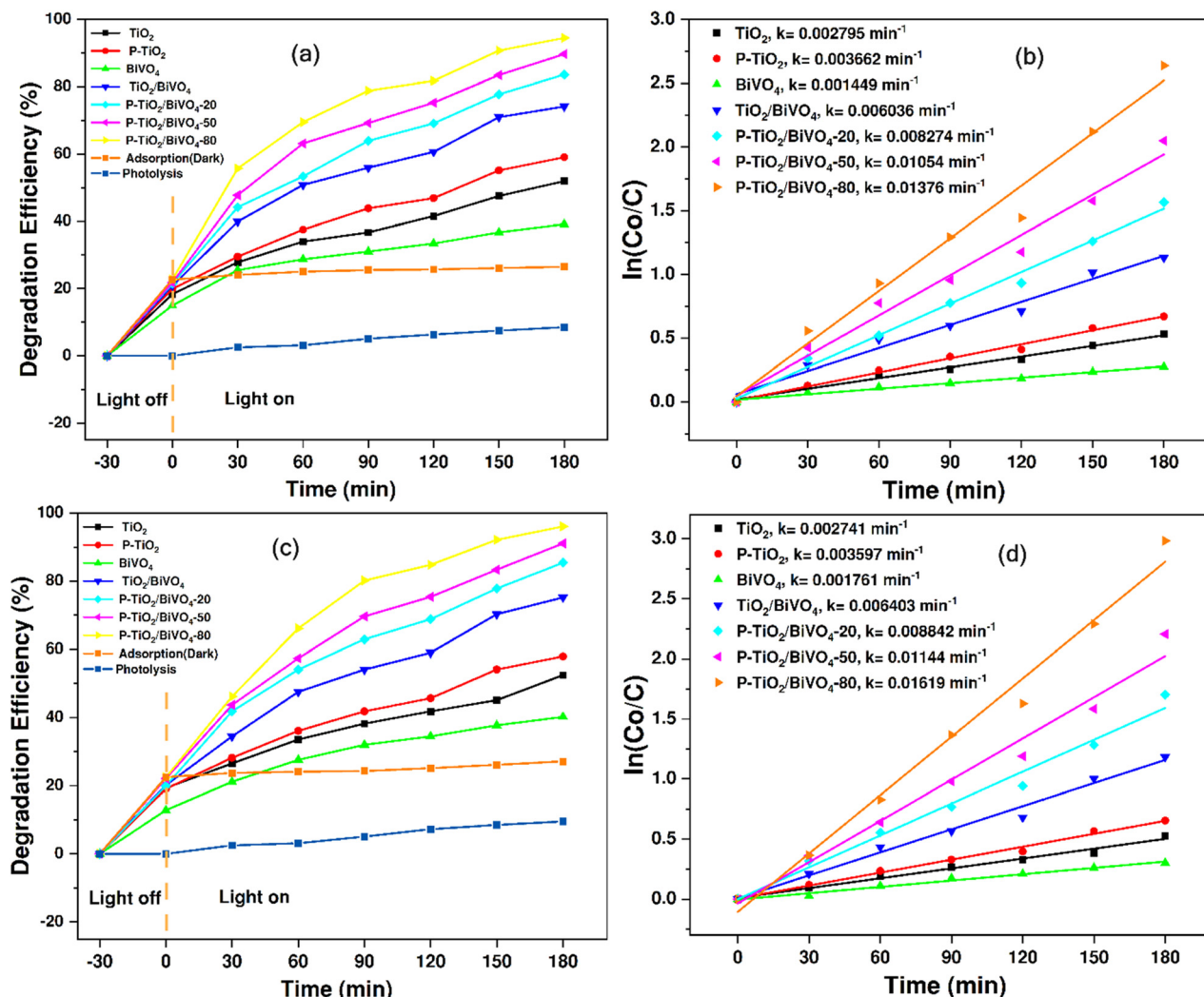


Fig. 6 Photocatalytic degradation of (a) CIP and (c) MNZ, and the kinetic study of (b) CIP and (d) MNZ for the synthesized composites (experimental conditions: 20 mg L⁻¹ of CIP/MNZ concentration, 1 g L⁻¹ of catalyst dosage, natural pH).

hole recombination by incorporating NiSe₂ resulted in 89% degradation of CIP within 120 minutes of treatment, whereas WO₃ removed 48%.

Among the three composites, the highest degradation efficiencies were observed for P-TiO₂/BiVO₄-80, which effectively degraded 94.48% of CIP and 96.07% of MNZ. This composite constitutes 80% of P-TiO₂ by mass; the properties of the P-TiO₂ are dominant here. Notably, as the proportion of BiVO₄ increased in P-TiO₂/BiVO₄ composites, the photodegradation of CIP and MNZ was reduced. This can be attributed to the inherent shortcomings of BiVO₄, including poor photogenerated electron mobility due to its lower bandgap, and reduced adsorption capacity and active sites associated with larger crystallite sizes.²³ Moreover, excess BiVO₄ can impede UV absorption by blocking the active sites of P-TiO₂, thereby hindering electron-hole separation at the heterojunction.²⁵ Thus, the dominant effect of BiVO₄ resulted in poor performances among the heterostructures. While P-TiO₂/BiVO₄-80 had an optimal bandgap (2.59 eV), it exhibited the smallest

crystallite size (14 nm) among the heterostructures, enabling higher adsorption capacities and enhanced effective photogenerated electron-hole mobility. Thus, we report the enhanced photocatalytic activity of the synthesized heterostructured photocatalysts, with an optimal preparation ratio of 80% P-TiO₂ and 20% BiVO₄.

3.3.2. Kinetic modelling. The photocatalytic degradation data for CIP and MNZ are fitted to zero-order, 1st-order, and 2nd-order rate kinetic models for all seven photocatalysts, using the linear models presented in Section 2.3.3. The R^2 values of the models are used as indicators of goodness of fit. The R^2 values and rate constants of all catalysts, for both CIP and MNZ degradation, are tabulated in Tables S2 and S3. All models achieved $R^2 \geq 0.90$; however, in the heterostructures, model deviations were substantially higher. Based on the R^2 values, the 1st-order kinetic model is best suited to all seven photocatalysts for both CIP and MNZ degradation ($R^2 > 0.98$). Heterogeneous catalysis typically follows first-order/pseudo-first-order models, derived from



the Langmuir–Hinshelwood expression. Thus, the photodegradation rate doesn't depend on catalyst loading or other factors; it depends solely on antibiotic concentration. All 1st-order rate constants for the degradation of CIP and MNZ with seven catalysts are shown in Fig. 6b and c. The apparent rate constant (k_a) of CIP degradation for P-TiO₂/BiVO₄-80 was 0.01376 min⁻¹, which is 4.92, 3.75, and 9.50 times higher than those for pristine TiO₂, P-TiO₂, and BiVO₄, respectively. This pattern is also observed for MNZ degradation, with the rate constant for P-TiO₂/BiVO₄-80 being 9.17 and 4.50 times that of BiVO₄ and P-TiO₂, respectively. Moreover, P-TiO₂/BiVO₄-80 showed 1.66- and 1.3-fold higher CIP degradation rates and 1.84 and 1.42-fold higher MNZ degradation rates than the TiO₂/BiVO₄-20 and TiO₂/BiVO₄-50 composites. This reaffirms our discussion of the superior degradation rate achieved by TiO₂/BiVO₄-80 compared with the others, further indicating that the formation of an optimal heterojunction between BiVO₄ and P-TiO₂ notably improves the photocatalytic performance for the removal of CIP and MNZ. Based on the kinetic analysis, the concentration profiles of CIP and MNZ can be expressed as $C_{(CIP,t)} = C_{(CIP,i)}(1 - \%ads)e^{(-0.01376t)}$ and $C_{(MNZ,t)} = C_{(MNZ,i)}(1 - \%ads)e^{(-0.01619t)}$. Here, C_t is the concentration at any time, C_i is the initial antibiotic concentration, %ads is the adsorption that can be found after achieving the adsorption–desorption equilibrium under dark conditions, and t is the time (min) after UV irradiation.

3.3.3. Performance modeling: catalytic potential, relative contribution, and synergy index. Given the superior performance of P-TiO₂/BiVO₄-80, as discussed in 3.3.1 and 3.3.2, we conducted a more detailed analysis of this heterostructure photocatalyst. Heterogeneous catalysis encompasses surface adsorption, UV photolysis, and the oxidative potential of photocatalysts. For both CIP and MNZ degradation, the progress of UV photolysis, the sole surface adsorption by P-TiO₂/BiVO₄-80, and the combined degradation over 180 minutes of treatment can be compared in Fig. 6a and c. It is evident that the overall degradation of CIP and MNZ was consistently higher than that *via* photolysis and surface adsorption. Thus, there is a clear synergy between the photocatalyst and the UV irradiation and adsorption. Thus, to understand the extent to which UV photolysis, surface adsorption, and photocatalysis contribute to the overall removal of antibiotics, the relative contribution (RC) to total removal, catalytic potential (CP), and synergy index (SI) are evaluated, as described in the Methodology section. These parameters are commonly used as the performance indicators of heterogeneous catalysis.

For 180 minutes of CIP treatment, 5.51 ± 2.2% removal was due to UV photolysis, and 25.50 ± 0.77% was from surface adsorption (Fig. 6a). The estimated CP of P-TiO₂-BiVO₄-80 was 47.48 ± 10.2%, indicating that the photocatalyst addition resulted in, on average, a 47.5% increase in degradation efficiency over that achievable by sole adsorption and photolysis. Hence, the coupled photocatalysts exhibit a synergistic effect across these hybrid processes. For MNZ, the trend is similar, with an estimated CP of 46.50 ± 12.45%, reaffirming the superior activity of the P-TiO₂/BiVO₄-80 photocatalyst coupled with photolysis.

Now, the contribution of each process to the total degradation can be further visualized using relative contribution (RC) analysis. Among the total CIP degradation, UV photolysis and surface adsorption accounted for 9% and 28%, respectively, and the remaining 63% was attributed to the photocatalyst's oxidative activity. For MNZ degradation, the pattern is similar: 9.90% and 28.22% are attributed to photolysis and adsorption, whereas the majority of degradation (61.88%) is due to photocatalytic activity. Although photogenerated radicals primarily contribute to antibiotic degradation, surface adsorption plays a crucial role in the overall degradation process by bringing pollutants to active sites, after which subsequent degradation occurs. Thus, from the CP and RC analyses, the synergistic adsorption–degradation process and its benefits in achieving high degradation performance are evident.

Now, to understand whether it is beneficial or to what extent the coupling of P-TiO₂ with BiVO₄ helped to obtain higher photocatalytic performance, the synergy index (SI) values of the TiO₂/BiVO₄-80 heterostructure are calculated for the CIP and MNZ degradation. Noting the positive, SI ≥ 1 indicates the positive synergy of coupling P-TiO₂ with BiVO₄ and with the UV photolysis, and SI ≤ 1 indicates ineffective coupling. For 180 minutes of CIP and MNZ treatment, the SI values of P-TiO₂-BiVO₄-80 are estimated to be 1.09 ± 0.03 and 1.10 ± 0.06, respectively. This confirms the synergistic nature of coupling P-TiO₂ with BiVO₄ in the UV system for the efficient removal of the antibiotics. This also ratifies that P-TiO₂-BiVO₄-80 can successfully harness the benefits of both P-TiO₂ and BiVO₄, as discussed in Section 3.3.1, as well as those of UV-mediated photocatalysis.

3.3.4. Effect of the operational parameters. In addition to the photocatalyst's properties, heterogeneous photocatalysis is strongly influenced by external operational parameters, most notably solution pH, pollutant initial concentration, catalyst dose, external oxidants (*e.g.*, per- and monosulfates and peroxides), and external ions. It is imperative to analyze the effects of these parameters to determine the optimal operational conditions for achieving maximum degradation efficiency. Here, the effects of solution pH, initial antibiotic concentrations (CIP and MNZ), and peroxide are studied for the best photocatalyst P-TiO₂/BiVO₄-80. Moreover, the degradation of MNZ and CIP under different operating conditions was fitted to first-order reaction kinetics. The kinetic parameters and R^2 values are summarized in Table S4.

3.3.4.1. Effect of pH. The impact of the change of the solution pH on the photodegradation (both for CIP and MNZ) was studied by varying the solution pH at 3, 10, and the natural pH of the antibiotics (6.5 for CIP and 6.3 for MNZ), while the photocatalyst loading was kept at 1 g L⁻¹ and the antibiotic concentration at 20 ppm. The degradation profiles of CIP and MNZ across these pH ranges are shown in Fig. 7, along with the corresponding kinetic models. For CIP, the highest degradation was observed under natural pH conditions (94.5%), approximately 15% and 6.4% higher than that at pH 3 and 10, respectively. CIP exists primarily as a zwitterionic structure



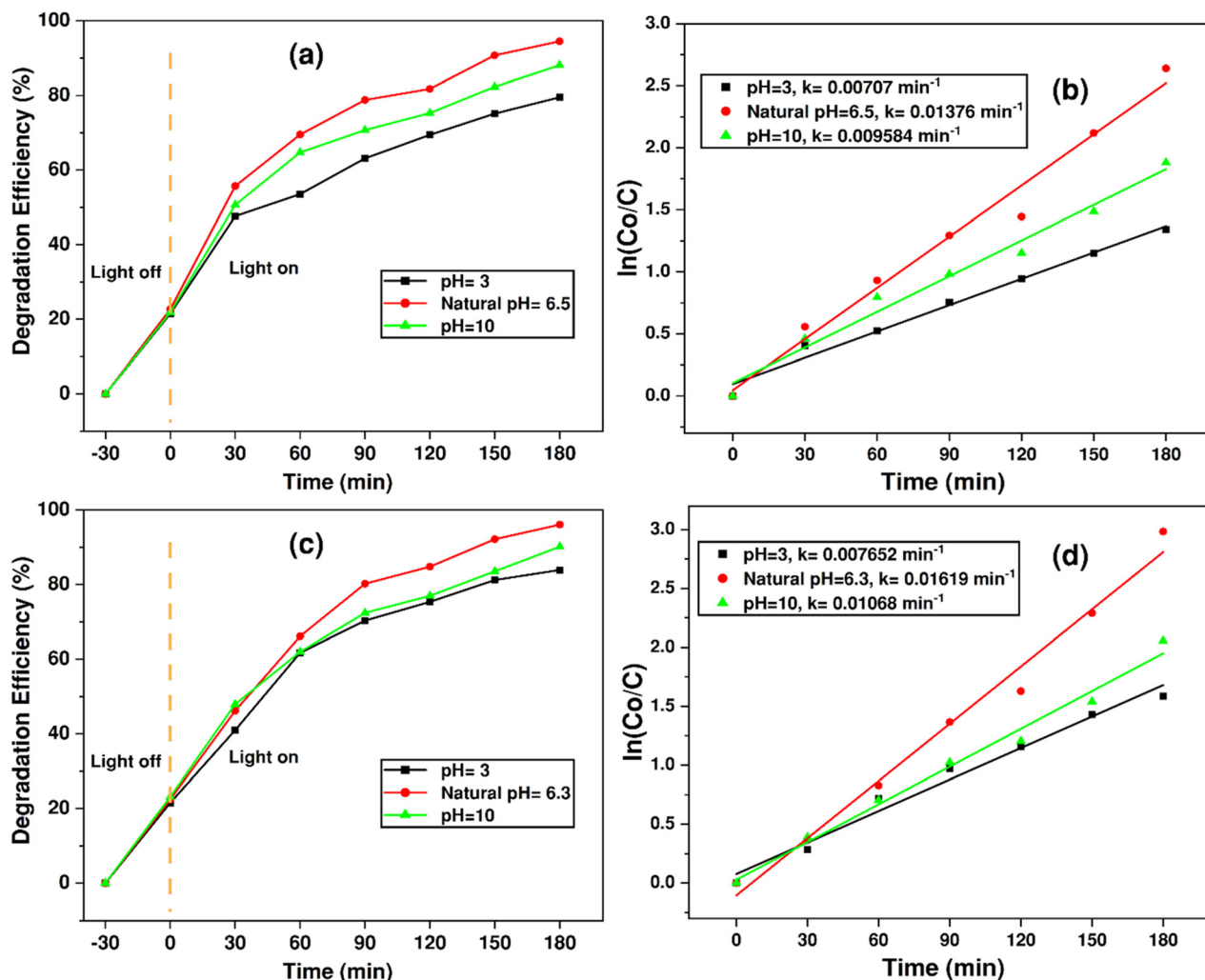


Fig. 7 Photocatalytic degradation of (a) CIP, (c) MNZ, and kinetic models for (b) CIP and (d) MNZ for different initial solution pH values using P-TiO₂/BiVO₄-80 (experimental conditions: 20 mg L⁻¹ of pollutant concentration and 1 g L⁻¹ catalyst dosage).

with both carboxylic acid and piperazine groups, giving two pK_a values at pK_{a1} 6.1 and pK_{a2} = 8.7. Therefore, the CIP molecules are positively charged at pH below 6.1 and negatively charged at pH above 8.7. Since the calculated point of zero charge (PZC) of the catalyst is 6.31 (Fig. S10), electrostatic repulsion between CIP and the catalyst surface at both acidic and basic pH, hinders the adsorption.³⁷ This is why photodegradation is faster at neutral pH (1.68 and 1.50 times higher than at pH 3 and pH 10), as shown in Fig. 7(a and b). Moreover, photodegradation at basic pH (pH 10) was higher than that at acidic pH, owing to the readily available hydroxide ion, which facilitates the formation of OH[•] as a key component of the AOP.

On the other hand, although MNZ is zwitterionic, its structure, with a highly negative nitro group, makes it a polar compound with a pK_a of 2.87. Hence, it is cationic at pH < 2.87 and anionic at pH > 2.87. The MNZ degradation is also maximal at the antibiotic's natural pH (pH 6.3), degrading 96% of MNZ within 180 minutes, whereas the degradation was 84% and 90.2% at pH 3 and pH 10, respectively. The rate of degradation at natural pH was 1.82 and 1.52 times higher than

that at pH 3 and pH 10 (Fig. 7c and d). The low degradation at pH 3 is attributable to the scarcity of hydroxide ions. Moreover, particles tend to agglomerate at acidic pH, whereas at basic pH, electrostatic repulsion between the photocatalyst surface and MNZ reduces adsorption.³⁸

3.3.4.2. Effect of initial antibiotic concentration. Additionally, the effects of initial concentrations on the degradation of MNZ and CIP, as well as on the corresponding rate constants, are illustrated in Fig. 8. The antibiotic concentrations were varied from 10 to 30 mg mL⁻¹ for CIP and MNZ, while the catalyst loading was maintained at 1 g L⁻¹ and at the natural pH of the antibiotics. The maximum degradation of both CIP and MNZ occurred at 10 mg L⁻¹, and the corresponding rate constants were also highest. At this initial concentration, the CIP degradation efficiency was 96%, and the rate constant was 1.67 times that at 30 mg L⁻¹. The same trend was observed for MNZ degradation. The degradation efficiency of MNZ at an initial concentration of 10 mg L⁻¹ was 98.24%. The lower degradation at higher concentrations is mainly due to the scarcity of OH[•],



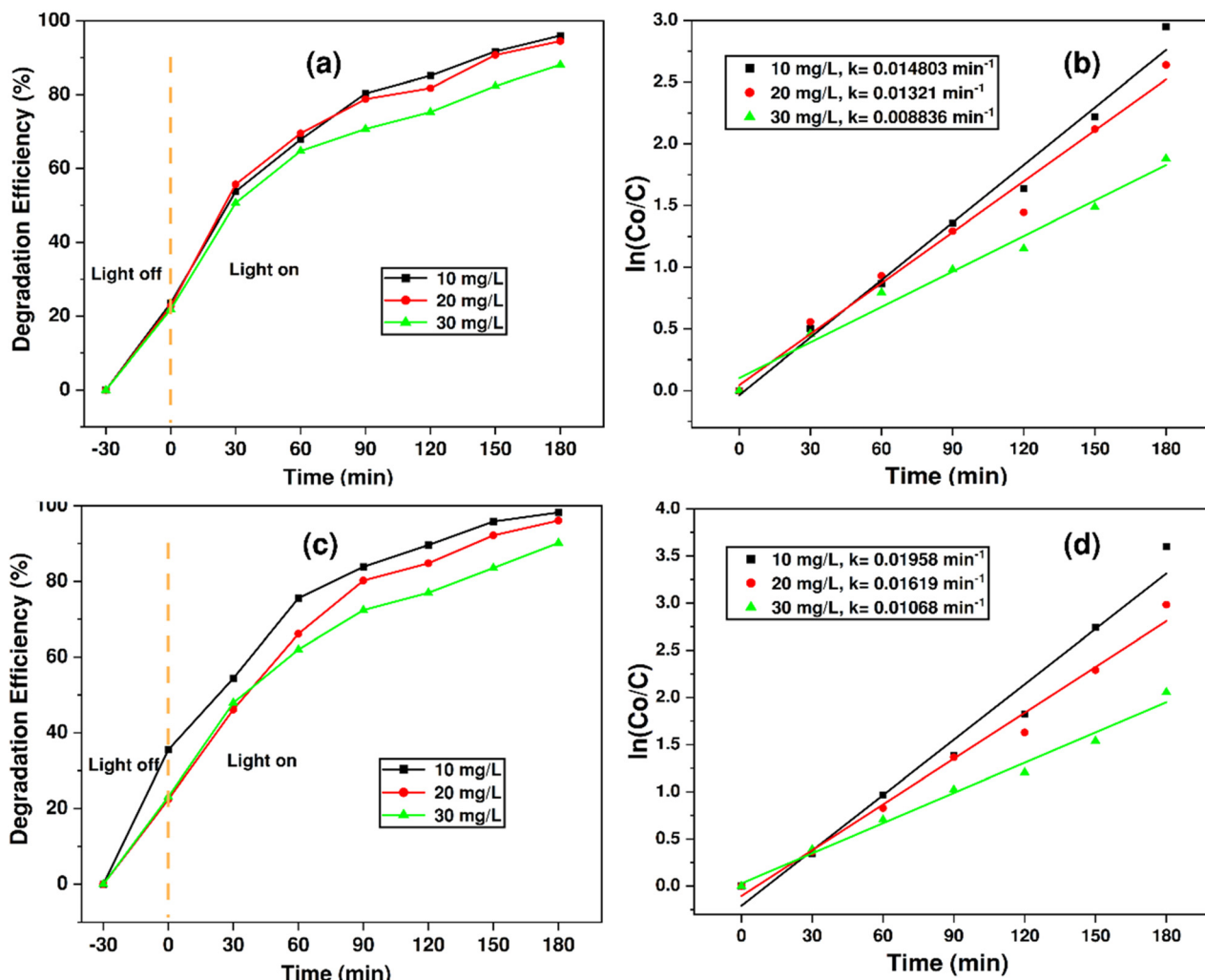


Fig. 8 Photocatalytic degradation of (a) CIP and (c) MNZ, and kinetic models for (b) CIP and (d) MNZ for different pollutant concentrations using P-TiO₂/BiVO₄-80 (experimental conditions: 1 g L⁻¹ catalyst dosage and natural pH).

O₂^{•-}, and other oxidative radicals, since the catalyst amount remains constant.³⁹ Moreover, higher pollutant concentrations saturate the active sites on the catalyst surface, thereby hindering adsorption.^{40,41} This is also evident from the total obtained adsorption of CIP and MNZ after exposure to the dark conditions. As pollutant concentration increased, adsorption capacity decreased for both CIP and MNZ.

3.3.4.3. Effect of catalyst dose. Fig. 9 demonstrates how the photodegradation of CIP and MNZ varies with changes in photocatalyst dosages (0.8, 1, 1.2, and 1.4 g L⁻¹), while keeping the other treatment parameters constant. For both CIP and MNZ, degradation increased as the catalyst concentration rose from 0.8 g L⁻¹ to 1.2 g L⁻¹ and then decreased when the catalyst dosage was further increased to 1.4 g L⁻¹. The maximum degradation for CIP and MNZ was 96.4% and 98.3%, respectively, for 1.2 g L⁻¹; therefore, the optimum catalyst dosage is 1.2 g L⁻¹. The degradation efficiency increases with catalyst dose up to a certain extent because of a greater number of available active sites for adsorption and the availability of

oxidative radicals for degradation. However, as the dosage increases further, degradation decreases because the particles impede radiation penetration, thereby reducing the exposure of active sites to UV light.⁴² This turbidity of the suspension affects charge-carrier separation by reducing UV penetration to active sites. Therefore, the degradation rate decreases with increasing catalyst dosage.^{43,44}

3.3.4.4. Effect of peroxide dose. External oxidizing agents can substantially alter the photocatalyst's degradation rate. In many heterogeneous catalytic AOPs, peroxides (H₂O₂), peroxymonosulfate (PMS, HSO₅⁻), ozone (O₃), and persulfate (S₂O₈²⁻) are used to mediate the oxidation process. These, upon UV irradiation, greatly facilitate the formation of highly reactive hydroxyl and sulfate radicals and enhance the degradation of organic pollutants.^{26,45} Thus, we employed H₂O₂ to assess the impact of external oxidizing agents on the overall degradation of CIP and MNZ, by varying H₂O₂ doses (10 mM, 20 mM, and 30 mM) while maintaining other operational parameters constant (Fig. S11).



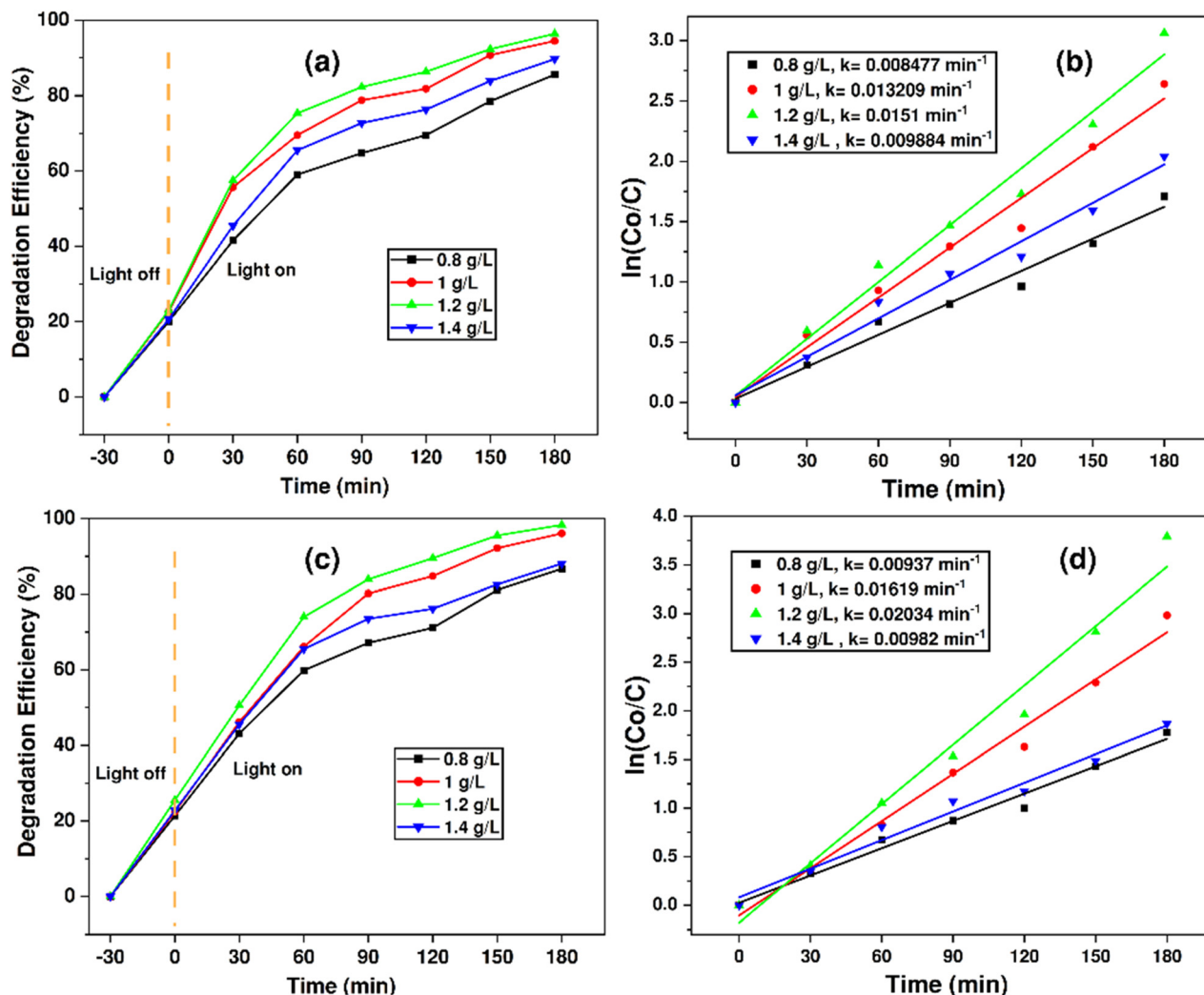
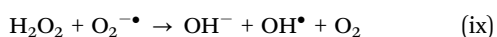
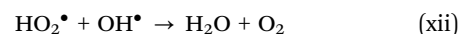
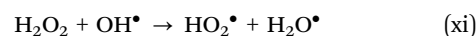


Fig. 9 Photocatalytic degradation of (a) CIP and (c) MNZ and kinetic models of (b) CIP and (d) MNZ for different catalyst dosages using P-TiO₂/BiVO₄-80 (experimental conditions: 20 mg L⁻¹ initial pollutant concentration and natural pH).

The degradation increases with H₂O₂ concentration up to 20 mM for both MNZ and CIP and then decreases at 30 mM. Nearly complete degradation of both MNZ and CIP was achieved at a H₂O₂ concentration of 20 mM. For CIP, the maximum rate constant of 0.02691 min⁻¹ was observed at 20 mM H₂O₂, decreasing to 0.01192 min⁻¹ at 30 mM. On the other hand, the highest rate constant, 0.02511 min⁻¹, was observed at 20 mM MNZ, decreasing to 0.01135 min⁻¹ as the H₂O₂ concentration increased to 30 mM. Initially, the degradation rate increased because H₂O₂ acted as an electron scavenger, thereby reducing electron-hole recombination and hydroxyl radical formation, as shown in eqn (VIII).⁴⁶ In addition, H₂O₂ present in the system can aid in the generation of hydroxyl radicals by reacting with superoxide radicals as per eqn (ix).⁴⁷ Alongside, H₂O₂ itself can split to form OH[•] upon excitation by UV radiation (eqn (x)).⁴⁸



However, the presence of excess H₂O₂ resulted in the formation of less active hydroperoxyl radicals (HO₂[•]) and inhibited the formation of OH[•] (eqn (xi) and (xii)). This can retard the reaction rate.⁴⁹ This is why the overall degradation of CIP and MNZ decreased as the H₂O₂ concentration increased to 30 mM.



Moreover, the degradation experiments were conducted in the absence of a catalyst using 20 mM H₂O₂ under UV-A radiation, yielding degradation efficiencies of 11.51% and 14.31% for CIP and MNZ, respectively. This UV photolysis with H₂O₂ was lower since it requires lower irradiation wavelengths for free radical formation, and there is no adsorption of the pollutants.⁵⁰

3.3.5. Degradation performance in the binary antibiotic mixture. The preceding sections addressed the enhanced catalytic performance of the synthesized photocatalyst for



individual CIP and MNZ solutions, as well as the superior performance of P-TiO₂/BiVO₄-80. However, real wastewater contains multiple antibiotics that must be treated simultaneously. Additionally, due to the different molecular structures and physicochemical behaviours of the pollutants, photodegradation can be synergistic, and adsorption and subsequent degradation can be competitive.²⁶ Thus, for robust photocatalyst design, the degradation performance in binary or ternary pollutant mixtures is imperative to analyze. Hence, the photocatalytic performance of TiO₂/BiVO₄-80 in a CIP and MNZ mixture was evaluated by keeping the concentration of the pollutants at 15 mg L⁻¹, with 1 g L⁻¹ of catalyst loading, natural pH, and in the presence of 20 mM of H₂O₂ dose. The performance is illustrated in Fig. 10. Both MNZ and CIP degradation was excellent, achieving 97.76% and 94.56% after 180 minutes of UV irradiation, which is very close to their individual degradation performance under the same treatment conditions. The total degradation and degradation rate ($k = 0.019822 \text{ min}^{-1}$) for MNZ were slightly higher compared to that for CIP ($k = 0.015333 \text{ min}^{-1}$), which was also observed for individual degradation performance. This may be attributed to differences in their structure and physicochemical properties.

The presence of the nitro (-NO₂) group in the structure of MNZ makes it more susceptible to photocatalytic degradation.⁵¹ On the other hand, CIP has a complex fluoroquinolone structure, which makes it comparatively more stable than MNZ.⁵² Here, the degradation in the binary mixture differs little from that in the single solution. Thus, there is no synergistic effect or suppression of photodegradation in the binary solution of CIP and MNZ. This behavior was also reported for the homogeneous AOP, using persulfate-peroxide for the photodegradation of CIP and MNZ.²⁶ Thus, the synthesized TiO₂/BiVO₄-80 can be used for the simultaneous removal of multiple antibiotics from wastewater.

3.3.6. Recyclability. The stability of P-TiO₂/BiVO₄-80 was evaluated by recycling the catalysts for five cycles in the binary

mixture of CIP and MNZ, as shown in Fig. 11. In the binary mixture, the pollutant concentration was maintained at 15 mg L⁻¹, the catalyst dose at 1 g L⁻¹, and the H₂O₂ concentration at 20 mM for 180 minutes. The degradation efficiencies for MNZ and CIP declined from 97.76% and 94.56% to 81.11% and 78.13%, respectively, after five cycles, corresponding to approximately 3.30% reduction per cycle for both antibiotics. The decrease in photocatalytic activity is primarily due to the blocking of available active sites by intermediate products and structural changes.⁵³ However, the loss of photocatalytic activity is not significant, indicating the stability of the photocatalyst sample.

3.4. Photocatalytic degradation mechanism

The photocatalytic degradation mechanism of MNZ and CIP using the synthesized P-TiO₂/BiVO₄ composite is depicted in Fig. 12. Under UV irradiation and upon adsorption on the composite, electron-hole pair separation occurs in P-TiO₂ and BiVO₄. For P-doped TiO₂, the substitution of Ti⁴⁺ by P⁵⁺ results in shallow donor states (P 3p) below the conduction band of TiO₂.⁵⁴ The transfer is mainly due to the relative positions of the CBs. The holes are transferred from the VB of BiVO₄ to the more negatively positioned VB of P-TiO₂.⁵⁵ This separation of electron-hole pairs reduces recombination. Moreover, the effective band gap of the heterojunction is also reduced as P-TiO₂/BiVO₄-80 has a band gap of 2.59 eV. The photogenerated holes react with adsorbed water and hydroxide molecules to generate OH• radicals, and the electrons interact with electron scavengers, such as dissolved O₂, to generate O₂•⁻ radicals. These O₂•⁻ radicals act as strong oxidizing agents and undergo further reactions to form OH• radicals eventually. Thus, adsorbed CIP and MNZ molecules react with the formed OH• and O₂•⁻, resulting in the formation of degradation products such as CO₂ and H₂O. The transfer of electron-hole pairs at a heterojunction inhibits electron-hole separation and reduces

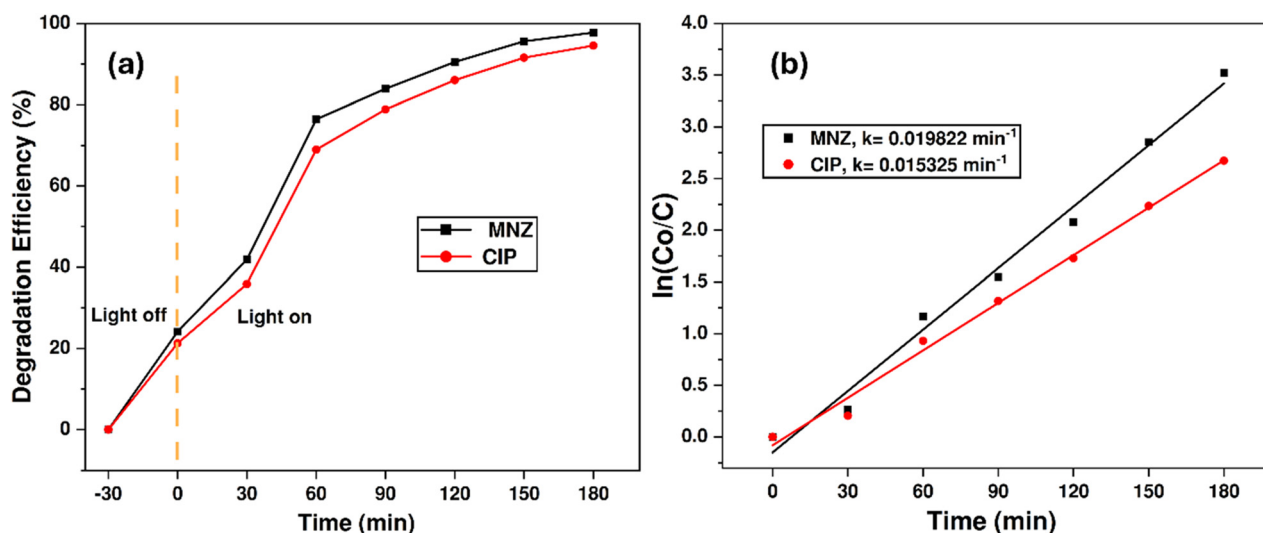


Fig. 10 (a) Degradation efficiency vs. time and (b) first-order kinetic models for the binary antibiotic mixture (experimental conditions: [CIP]₀ = [MNZ]₀ = 15 mg L⁻¹, 1 g L⁻¹ catalyst dosage, [H₂O₂]₀ = 20 mM, natural pH).



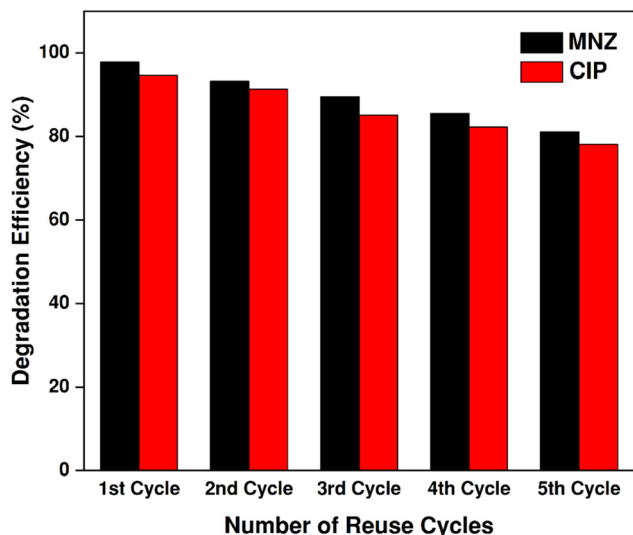


Fig. 11 Reusability of P-TiO₂/BiVO₄-80 for 5 cycles (experimental conditions: [CIP]₀ = [MNZ]₀ = 15 mg L⁻¹, 1 g L⁻¹ catalyst dosage, [H₂O₂]₀ = 20 mM, natural pH).

the band gap, thereby facilitating the degradation of adsorbed antibiotic molecules.

4. Concluding remarks, study shortfalls, and way forward

This study systematically investigated the photocatalytic performance of a novel P-doped TiO₂/BiVO₄ heterostructure photocatalyst, both for individual and binary mixtures of CIP and MNZ antibiotics.

The characterization revealed that the incorporation of anatase TiO₂ and monoclinic BiVO₄ substantially benefited from the favorable features of both, with reduced crystal size and improved surface roughness, leading to higher adsorption

capacity, an optimized bandgap, and excellent photogenerated electron-hole transfer. Among the synthesized composites, P-TiO₂/BiVO₄-80 exhibited superior photocatalytic performance, with an optimal crystal size of 14 nm and a band gap of 2.59 eV, achieving degradation efficiencies exceeding 94% for CIP and 96% for MNZ under UV-A irradiation. In addition, two multivariable linear regression models were developed to predict the crystal structure size and the bandgap from elemental composition. The estimated catalytic potential and the synergy index showed the effectiveness of coupling P-TiO₂ with BiVO₄ for potential use in AOPs. The photocatalyst exhibited excellent performance in a binary mixture of CIP and MNZ, with a degradation rate comparable to that observed for the individual antibiotics. Moreover, the photocatalyst demonstrated excellent reusability, maintaining over 78% efficiency after five cycles.

This is the first attempt to investigate this novel photocatalyst as a potential solution for the degradation of recalcitrant pollutants in surface water; however, the study has some shortcomings that can guide future improvements to this material for large-scale implementation. Here, we discussed some limitations and suggested future directions for detailed investigation.

- In this study, the material characterization was done using FESEM-EDX, XRD, FTIR, and UV-vis, which couldn't provide more detailed information on the structural and functional properties of the synthesized catalyst. Advanced spectroscopic and electrochemical techniques, such as transient photocurrent responses and electrochemical impedance spectroscopy, could further elucidate charge-transfer dynamics under different illumination regimes. TEM and TGA can provide essential insights into the successful doping and the thermal stability of the materials. Thus, we suggest further exploration of these.

- Photocatalytic experiments were conducted under controlled UV-A irradiation. While this approach allowed isolation

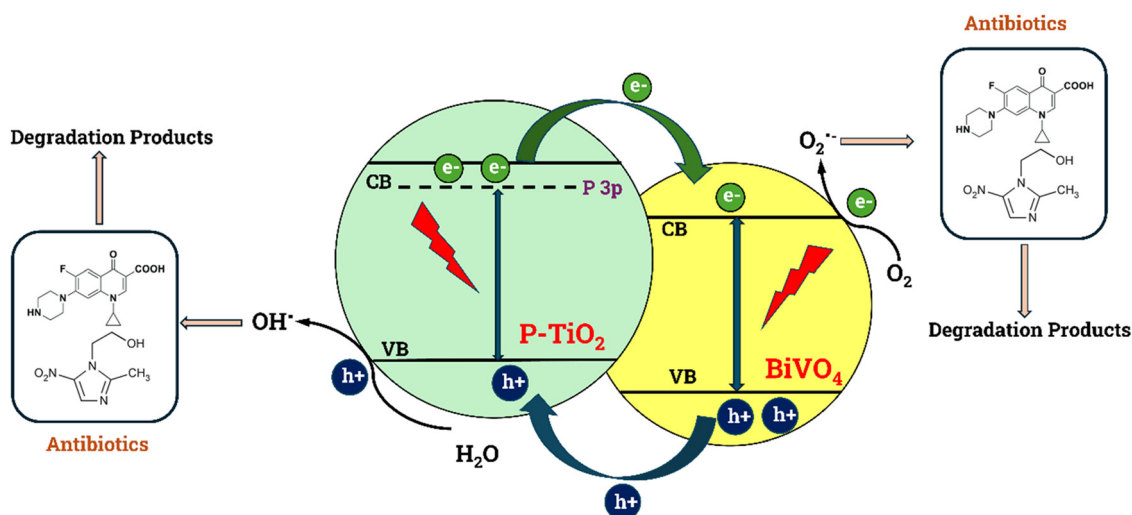


Fig. 12 Degradation mechanism of P-TiO₂/BiVO₄ for the degradation of antibiotics.



of intrinsic heterojunction effects and reliable benchmarking against TiO₂-based systems, it did not fully represent solar-driven operation. Although the composite exhibited a reduced band-gap energy within the visible-light utilization range, the contribution of solar irradiation to long-term degradation efficiency was not analyzed in this initial study. Thus, further investigation of P-TiO₂/BiVO₄ under visible-light and simulated solar irradiation is required to assess its applicability to real effluents containing natural organic matter, inorganic ions, and competing radical scavengers.

- This study primarily focused on parent compound removal to investigate the catalytic potential of this synthesized novel composite; mineralization extent and the toxicity of transformation intermediates were not comprehensively evaluated. Additionally, UV-vis-based concentration determination for degradation has a well-known limitation: it can overestimate the parent compound if the intermediates have the same absorption wavelength, and this method doesn't provide information about partially degraded intermediates. Moreover, partial degradation may still yield biologically active or toxic by-products, thereby limiting direct environmental risk assessment. Thus, comprehensive mineralization studies, including total organic carbon (TOC) analysis, identification of degradation intermediates *via* HPLC or LC-MS analysis, and toxicity assessment of degradation by-products, can help ensure environmental safety and elucidate degradation mechanisms.

- From the practical viewpoint, the large-scale implementation of powder photocatalysts in a wastewater treatment plant is associated with post-processing difficulties, mass loss, turbidity, separation, and recycling issues. The immobilization, specifically biopolymer-based immobilization, provides a solution to these problems, with an additional enhancement in pollutant uptake capacity through a synergistic adsorption-degradation mechanism.³³ Further studies of our synthesized photocatalyst immobilized in biopolymer hydrogel matrices (chitosan, alginate, carboxymethyl cellulose, PVA, PANI, *etc.*) can provide an efficient means for efficient absorber and photocatalytic reactor design. In addition, the benefits, sustainability, and large-scale feasibility of the synthesized P-TiO₂/BiVO₄ photocatalyst can be evaluated through techno-economic analysis (TEA) integrated with life cycle analysis (LCA). Sometimes, nanomaterials show significant improvements in energy requirements in smaller-scale processes but exhibit substantial energy consumption during synthesis and preparation and throughout the life cycle.^{12,56} Thus, an integrated TEA-LCA with hotspot analysis can be conducted to identify energy-intensive routes, improve energy efficiency, and reduce the environmental footprint.

Overall, this study offers significant insights into the development of a highly efficient P-TiO₂/BiVO₄ photocatalyst, which holds great promise for removing antibiotics and other persistent organic pollutants from water. We believe that the proposed future work in these directions would benefit the transition toward sustainable wastewater treatment, reduce the environmental footprint, and help ensure clean water availability for everyone.

Author contributions

Tanzim Ur Rahman: writing – methodology, investigation, data collection, data analysis, and original draft; Musfekur Rahman Dihan: writing – methodology, data analysis, and original draft, review and editing; Abdul Hai: review and editing; Md. Shahinor Islam: review and editing, supervision.

Conflicts of interest

The authors declare that they have no known competing financial interests or personal relationships that could have appeared to influence the work reported in this paper.

Data availability

Data obtained from the laboratory based experiments were used to produce figures, and analysis and the remaining data are included in the supplementary information (SI). Supplementary information is available. See DOI: <https://doi.org/10.1039/d5ma01398d>.

Further availability of the data will be provided upon request to the corresponding author.

Acknowledgements

This research project was funded by the CASR Postgraduate Research Fund, Bangladesh University of Engineering and Technology (BUET), and BUET Chemical Engineering Forum (BCEF). The authors would like to acknowledge the laboratory support from the Department of Chemical Engineering, Bangladesh University of Engineering and Technology (BUET), Dhaka, Bangladesh.

References

- 1 F. Mahmud, T. S. Banhi, H. Roy, M. R. Dihan, Md. S. Islam and Y. Cai, *et al.*, Antibiotic-contaminated wastewater treatment and remediation by electrochemical advanced oxidation processes (EAOPs), *Groundw. Sustain. Dev.*, 2024, 25, 101181.
- 2 T. L. Yusuf, B. O. Ojo, T. Mushiana, N. Mabuba, O. A. Arotiba and S. Makgato, Synergistically enhanced photoelectrocatalytic degradation of ciprofloxacin via oxygen vacancies and internal electric field on a NiSe₂/WO₃ photoanode, *Catal. Sci. Technol.*, 2024, 14(20), 6015–6026.
- 3 A. J. Browne, M. G. Chipeta, G. Haines-Woodhouse, E. P. A. Kumaran, B. H. K. Hamadani and S. Zarea, *et al.*, Global antibiotic consumption and usage in humans, 2000–18: a spatial modelling study, *Lancet Planet. Health*, 2021, 5(12), e893–e904.
- 4 A. Guha Roy, Antibiotics in water, *Nat. Sustainability*, 2019, 2(5), 356.
- 5 F. Akter, M. R. Amin, K. T. Osman, M. N. Anwar, M. M. Karim and M. A. Hossain, Ciprofloxacin-resistant *Escherichia coli* in hospital wastewater of Bangladesh and



- prediction of its mechanism of resistance, *World J. Microbiol. Biotechnol.*, 2012, **28**(3), 827–834.
- 6 J. L. Wilkinson, A. B. A. Boxall, D. W. Kolpin, K. M. Y. Leung, R. W. S. Lai and C. Galbán-Malagón, *et al.*, Pharmaceutical pollution of the world's rivers, *Proc. Natl. Acad. Sci. U. S. A.*, 2022, **119**, 8.
 - 7 S. Akter, M. S. Islam, M. H. Kabir, M. A. A. Shaikh and M. A. Gafur, UV/TiO₂ photodegradation of metronidazole, ciprofloxacin and sulfamethoxazole in aqueous solution: An optimization and kinetic study, *Arabian J. Chem.*, 2022, **15**(7), 103900.
 - 8 T. U. Rahman, H. Roy, A. Fariha and A. Z. Shoronika, Al-Mamun MdR, Islam SZ, *et al.* Progress in plasma doping semiconductor photocatalysts for efficient pollutant remediation and hydrogen generation, *Sep. Purif. Technol.*, 2023, **320**, 124141.
 - 9 M. Sharma, D. Rajput, V. Kumar, I. Jatain, T. M. Aminabhavi and G. Mohanakrishna, *et al.*, Photocatalytic degradation of four emerging antibiotic contaminants and toxicity assessment in wastewater: A comprehensive study, *Environ. Res.*, 2023, **231**, 116132.
 - 10 M. Rashid Al-Mamun, M. Shofikul Islam, M. Rasel Hossain, S. Kader, M. Shahinoor Islam and M. Zaved Hossain Khan, A novel and highly efficient Ag and GO co-synthesized ZnO nano photocatalyst for methylene blue dye degradation under UV irradiation, *Environ. Nanotechnol., Monit. Manage.*, 2021, **16**, 100495.
 - 11 T. U. Rahman, H. Roy, A. Z. Shoronika, A. Fariha, M. Hasan and Md. S. Islam, *et al.*, Sustainable toxic dye removal and degradation from wastewater using novel chitosan-modified TiO₂ and ZnO nanocomposites, *J. Mol. Liq.*, 2023, **388**, 122764.
 - 12 M. R. Dihan, T. U. Rahman, M. A. J. R. Khan, T. S. Banhi, S. Sadaf and M. S. Reza, *et al.*, Photocatalytic and photoelectrochemical H₂ generation for sustainable future: Performance improvement, techno-economic analysis, and life cycle assessment for shaping the reality, *Fuel*, 2025, **392**, 134356.
 - 13 Q. Guo, C. Zhou, Z. Ma and X. Yang, Fundamentals of TiO₂ Photocatalysis: Concepts, Mechanisms, and Challenges, *Adv. Mater.*, 2019, **31**, 50.
 - 14 T. L. Yusuf, O. C. Olatunde, D. Masekela, K. D. Modibane, D. C. Onwudiwe and S. Makgato, Charge Redistribution in NiSe₂/MoS₂ n-n Heterojunction towards the Photoelectrocatalytic Degradation of Ciprofloxacin, *ChemElectroChem*, 2024, **11**(16), e202400309.
 - 15 X. Wang, L. L. Wang, D. Guo, L. L. Ma, B. L. Zhu and P. Wang, *et al.*, Fabrication and photocatalytic performance of C, N, F-tridoped TiO₂ nanotubes, *Catal. Today*, 2019, **327**(2010), 182–189.
 - 16 M. R. Al-Mamun, S. Kader, M. S. Islam and M. Z. H. Khan, Photocatalytic activity improvement and application of UV-TiO₂ photocatalysis in textile wastewater treatment: A review, *J. Environ. Chem. Eng.*, 2019, **7**, 5.
 - 17 L. G. Devi and R. Kavitha, A review on non metal ion doped titania for the photocatalytic degradation of organic pollutants under UV/solar light: Role of photogenerated charge carrier dynamics in enhancing the activity, *Appl. Catal., B*, 2013, **140–141**, 559–587.
 - 18 X. Feng, P. Wang, J. Hou, J. Qian, Y. Ao and C. Wang, Significantly enhanced visible light photocatalytic efficiency of phosphorus doped TiO₂ with surface oxygen vacancies for ciprofloxacin degradation: Synergistic effect and intermediates analysis, *J. Hazard. Mater.*, 2018, **351**, 196–205.
 - 19 N. O. Gopal, H. H. Lo, T. F. Ke, C. H. Lee, C. C. Chou and J. D. Wu, *et al.*, Visible Light Active Phosphorus-Doped TiO₂ Nanoparticles: An EPR Evidence for the Enhanced Charge Separation, *J. Phys. Chem. C*, 2012, **116**(30), 16191–16197.
 - 20 V. Liapun, M. B. Hanif, M. Sihor, X. Vislocka, S. Pandiaraj, U. V. K., G. K. Thirunavukkarasu, M. F. Edelmánová, M. Reli, O. Monfort, K. Kočí and M. Motola, *et al.*, Versatile application of BiVO₄/TiO₂ S-scheme photocatalyst: Photocatalytic CO₂ and Cr(VI) reduction, *Chemosphere*, 2023, **337**, 139397.
 - 21 H. Roy, T. U. Rahman, Md. A. J. R. Khan, Md. R. Al-Mamun, S. Z. Islam and Md. A. Khaleque, *et al.*, Toxic dye removal, remediation, and mechanism with doped SnO₂-based nanocomposite photocatalysts: A critical review, *J. Water Proc. Eng.*, 2023, **54**, 104069.
 - 22 B. Y. Cheng, J. S. Yang, H. W. Cho and J. J. Wu, Fabrication of an Efficient BiVO₄-TiO₂ Heterojunction Photoanode for Photoelectrochemical Water Oxidation, *ACS Appl. Mater. Interfaces*, 2016, **8**(31), 20032–20039.
 - 23 M. Liaqat, S. Kausar, T. Iqbal, S. Afsheen, A. Younas and M. Zubair, *et al.*, Synergistic Photocatalytic Activity of TiO₂/BiVO₄ Nanocomposites: Optimization, Characterization, and Recyclability for Dye and Antibiotic Degradation, *J. Inorg. Organomet. Polym. Mater.*, 2024, **34**(7), 3246–3257.
 - 24 S. Cipagauta-Díaz, A. Estrella-González, M. Navarrete-Magaña and R. Gómez, N doped -TiO₂ coupled to BiVO₄ with high performance in photodegradation of Ofloxacin antibiotic and Rhodamine B dye under visible light, *Catal. Today*, 2022, **394–396**, 445–457.
 - 25 C. Wu, J. Dai, J. Ma, T. Zhang, L. Qiang and J. Xue, Mechanistic study of B-TiO₂/BiVO₄ S-scheme heterojunction photocatalyst for tetracycline hydrochloride removal and H₂ production, *Sep. Purif. Technol.*, 2023, **312**, 123398.
 - 26 M. R. Dihan, Md. A. Alam, S. Akter, Md. A. Gafur and Md. S. Islam, Statistical modeling and application of machine learning for antibiotic degradation using UV/persulfate-peroxide based advanced oxidation process, *Heliyon.*, 2025, **11**(13), e43664.
 - 27 M. R. Al-Mamun, S. Kader and M. S. Islam, Solar-TiO₂ immobilized photocatalytic reactors performance assessment in the degradation of methyl orange dye in aqueous solution, *Environ. Nanotechnol., Monit. Manage.*, 2021, **16**, 100514.
 - 28 R. Rescigno, O. Sacco, V. Venditto, A. Fusco, G. Donnarumma and M. Lettieri, *et al.*, Photocatalytic activity



- of P-doped TiO₂ photocatalyst, *Photochem. Photobiol. Sci.*, 2023, **22**(6), 1223–1231.
- 29 B. Xie, C. He, P. Cai and Y. Xiong, Preparation of monoclinic BiVO₄ thin film by citrate route for photocatalytic application under visible light, *Thin Solid Films*, 2010, **518**(8), 1958–1961.
- 30 K. T. Drisya, M. Solís-López, J. J. Ríos-Ramírez, J. C. Durán-Álvarez, A. Rousseau and S. Velumani, *et al.*, Electronic and optical competence of TiO₂/BiVO₄ nanocomposites in the photocatalytic processes, *Sci. Rep.*, 2020, **10**(1), 13507.
- 31 S. Y. Mendiola-Alvarez, Ma. A. Hernández-Ramírez, J. L. Guzmán-Mar, L. L. Garza-Tovar and L. Hinojosa-Reyes, Phosphorous-doped TiO₂ nanoparticles: synthesis, characterization, and visible photocatalytic evaluation on sulfamethazine degradation, *Environ. Sci. Pollut. Res.*, 2019, **26**(5), 4180–4191.
- 32 S. Y. Mendiola-Alvarez, M. A. Hernández-Ramírez, J. L. Guzmán-Mar, L. L. Garza-Tovar and L. Hinojosa-Reyes, Phosphorous-doped TiO₂ nanoparticles: synthesis, characterization, and visible photocatalytic evaluation on sulfamethazine degradation, *Environ. Sci. Pollut. Res.*, 2019, **26**(5), 4180–4191.
- 33 M. R. Dihan, S. Himel, Md. F. Abedin, S. M. A. Nayeem, A. A. Promy and Md. S. Islam, A Partial Air-Freeze Drying Strategy for TiO₂-Immobilized Chitosan Beads: Balancing Swelling and Stability for Improved Photocatalysis, *J. Mater. Res. Technol.*, 2025, **38**, 4115–4132.
- 34 V. Sivakumar, R. Suresh, K. Giribabu and V. Narayanan, BiVO₄ nanoparticles: Preparation, characterization and photocatalytic activity, ed A. M. Z. Slawin, *Cogent Chemistry*, 2015;vol. 1(1):1074647.
- 35 Y. Xia, Y. Jiang, F. Li, M. Xia, B. Xue and Y. Li, Effect of calcined atmosphere on the photocatalytic activity of P-doped TiO₂, *Appl. Surf. Sci.*, 2014, **289**, 306–315.
- 36 Md. R. Al-Mamun, Md. Z. Iqbal Rokon, Md. A. Rahim, Md. I. Hossain, Md. S. Islam and Md. R. Ali, *et al.*, Enhanced photocatalytic activity of Cu and Ni-doped ZnO nanostructures: A comparative study of methyl orange dye degradation in aqueous solution, *Heliyon.*, 2023, e16506.
- 37 A. Salma, S. Thoröe-Boveleth, T. C. Schmidt and J. Tuerk, Dependence of transformation product formation on pH during photolytic and photocatalytic degradation of ciprofloxacin, *J. Hazard. Mater.*, 2016, **313**, 49–59.
- 38 F. Bashiri, S. M. Khezri, R. R. Kalantary and B. Kakavandi, Enhanced photocatalytic degradation of metronidazole by TiO₂ decorated on magnetic reduced graphene oxide: Characterization, optimization and reaction mechanism studies, *J. Mol. Liq.*, 2020, **314**, 113608.
- 39 P. A. Mangrulkar, S. P. Kamble, M. M. Joshi, J. S. Meshram, N. K. Labhsetwar and S. S. Rayalu, Photocatalytic Degradation of Phenolics by N-Doped Mesoporous Titania under Solar Radiation, *Int. J. Photoenergy*, 2012, **2012**, 1–10.
- 40 B. Gupta, A. K. Gupta, C. S. Tiwary and P. S. Ghosal, A multivariate modeling and experimental realization of photocatalytic system of engineered S-C₃N₄/ZnO hybrid for ciprofloxacin removal: Influencing factors and degradation pathways, *Environ. Res.*, 2021, **196**, 110390.
- 41 A. K. Jha and S. Chakraborty, Photocatalytic degradation of tetracycline and ciprofloxacin antibiotic residues in aqueous phase by biosynthesized nZVI using Sal (*Shorea robusta*) leaf extract, *Aqua*, 2023, **72**(3), 230–245.
- 42 L. Zang, Photocatalytic Degradation of Water Pollutants Using Nano-TiO₂, *Green Energy and Technology*, Vol. 33, 2011.
- 43 M. A. Rauf and S. S. Ashraf, Fundamental principles and application of heterogeneous photocatalytic degradation of dyes in solution, *Chem. Eng. J.*, 2009, **151**(1–3), 10–18.
- 44 D. Zhao, J. Wang, Z. Zhang and J. Zhang, Photocatalytic degradation of omethoate using NaY zeolite-supported TiO₂, *Front. Chem. Eng. China*, 2009, **3**(2), 206–210.
- 45 M. H. Moslehi, M. S. Zadeh, K. Nateq, Y. D. Shahamat, N. A. Khan and N. Nasseh, Statistical computational optimization approach for photocatalytic-ozonation decontamination of metronidazole in aqueous media using CuFe₂O₄/SiO₂/ZnO nanocomposite, *Environ. Res.*, 2024, **242**, 117747.
- 46 Y. Zang and R. Farnood, Effect of Hydrogen Peroxide on the Photocatalytic Degradation of Methyl *tert*-butyl Ether, *Top. Catal.*, 2006, **37**(2–4), 91–96.
- 47 A. Touati, T. Hammedi, W. Najjar, Z. Ksibi and S. Sayadi, Photocatalytic degradation of textile wastewater in presence of hydrogen peroxide: Effect of cerium doping titania, *J. Ind. Eng. Chem.*, 2016, **35**, 36–44.
- 48 M. R. Al-Mamun, M. N. Karim, N. A. Nitun, S. Kader, M. S. Islam and M. Z. H. Khan, Photocatalytic performance assessment of GO and Ag co-synthesized TiO₂ nanocomposite for the removal of methyl orange dye under solar irradiation, *Environ. Technol. Innovation*, 2021, 22.
- 49 N. Bouanimba, R. Zouaghi, N. Laid and T. Sehili, Factors influencing the photocatalytic decolorization of Bromophenol blue in aqueous solution with different types of TiO₂ as photocatalysts, *Desalination*, 2011, **275**(1–3), 224–230.
- 50 G. S. Wang, C. H. Liao, H. W. Chen and H. C. Yang, Characteristics of natural organic matter degradation in water by UV/H₂O₂ treatment, *Environ. Technol.*, 2006, **27**(3), 277–287.
- 51 J. Sun, R. Chu and Z. U. H. Khan, A Theoretical Study on the Degradation Mechanism, Kinetics, and Ecotoxicity of Metronidazole (MNZ) in •OH- and SO₄•⁻-Assisted Advanced Oxidation Processes, *Toxics.*, 2023, **11**, 9.
- 52 P. P. Singh, G. Pandey, Y. Murti, J. Gairola, S. Mahajan and H. Kandhari, *et al.*, Light-driven photocatalysis as an effective tool for degradation of antibiotics, *RSC Adv.*, 2024, **14**(29), 20492–20515.
- 53 N. P. Rini, N. I. Istiqomah and E. Suharyadi, Enhancing photodegradation of methylene blue and reusability using CoO/ZnO composite nanoparticles, *Case Stud. Chem. Environ. Eng.*, 2023, **7**, 100301.
- 54 C. Sotelo-Vazquez, N. Noor, A. Kafizas, R. Quesada-Cabrera, D. O. Scanlon and A. Taylor, *et al.*, Multifunctional P-Doped TiO₂ Films: A New Approach to Self-Cleaning, Transparent



- Conducting Oxide Materials, *Chem. Mater.*, 2015, 27(9), 3234–3242.
- 55 Y. R. Lv, C. J. Liu, R. K. He, X. Li and Y. H. Xu, BiVO₄/TiO₂ heterojunction with enhanced photocatalytic activities and photoelectrochemistry performances under visible light illumination, *Mater. Res. Bull.*, 2019, 117, 35–40.
- 56 M. R. Dihan, T. Ahmed, T. U. Rahman, K. Bahar, N. M. Likhon, S. S. Sayem, *et al.*, in Sustainable nano-innovations at the heart of the water–energy–food nexus, *Climate Change Impacts on the Water-Energy-Food Nexus*, Elsevier, 2026, p. 539–56, Available from: <https://www.sciencedirect.com/science/article/pii/B978044322320400027X>.

